

# Constraints on the merging binary neutron star mass distribution and equation of state based on the incidence of jets in the population\*

Om Sharan Salafia<sup>1, 2, 3</sup>, Alberto Colombo<sup>1, 2</sup>, Francesco Gabrielli<sup>4</sup> and Ilya Mandel<sup>5, 6, 7</sup>

<sup>1</sup> Università degli Studi di Milano-Bicocca, Dip. di Fisica “G. Occhialini”, piazza della Scienza 3, I-20126 Milano (MI), Italy

<sup>2</sup> INFN – Sezione di Milano-Bicocca, piazza della Scienza 2, I-20126 Milano (MI), Italy

<sup>3</sup> INAF – Osservatorio Astronomico di Brera, via E. Bianchi 46, I-23807 Merate (LC), Italy

<sup>4</sup> Scuola Internazionale Superiore di Studi Avanzati (SISSA), via Bonomea 265, I-34136 Trieste (TS), Italy

<sup>5</sup> Monash Centre for Astrophysics, School of Physics and Astronomy, Monash University, Clayton, Victoria 3800, Australia

<sup>6</sup> ARC Center of Excellence for Gravitational Wave Discovery – OzGrav

<sup>7</sup> Institute of Gravitational Wave Astronomy and School of Physics and Astronomy, University of Birmingham, Birmingham, B15 2TT, United Kingdom

Draft, August 1, 2022

## ABSTRACT

A relativistic jet has been produced in the single well-localised binary neutron star (BNS) merger detected to date in gravitational waves (GWs), and the local rates of BNS mergers and short gamma-ray bursts are of the same order of magnitude. This suggests that jet formation is not a rare outcome for BNS mergers, and we show that this intuition can be turned into a quantitative constraint: at least about 1/3 of GW-detected BNS mergers, and at least about 1/5 of all BNS mergers, should produce a successful jet (90% credible level). Whether a jet is launched depends on the properties of the merger remnant and of the surrounding accretion disc, which in turn are a function of the progenitor binary masses and equation of state (EoS). The incidence of jets in the population therefore carries information about the binary component mass distribution and EoS. Under the assumption that a jet can only be produced by a black hole remnant surrounded by a non-negligible accretion disc, we show how the jet incidence can be used to place a joint constraint on the space of BNS component mass distributions and EoS. The result points to a broad mass distribution, with particularly strong support for masses in the  $1.3 - 1.6 M_{\odot}$  range. The constraints on the EoS are shallow, but we show how they will tighten as the knowledge on the jet incidence improves. We also discuss how to extend the method to include future BNS mergers, with possibly uncertain jet associations.

## 1. Introduction

Binary neutron star (BNS) mergers have long been considered (Eichler et al. 1989) as promising candidate progenitors of at least some gamma-ray bursts (GRBs). Evidence accumulated through the years pointing to the two observational GRB classes (‘long’ and ‘short’, Kouveliotou et al. 1993) being physically linked to two different progenitors, with collapsars (Woosley 1993) being the progenitors of long GRBs and BNS mergers (and possibly also neutron star - black hole mergers, Mochkovitch et al. 1993) being those of short GRBs (SGRBs, Berger 2014; D’Avanzo 2015). The confirmation of the collapsar progenitor scenario for long GRBs came with the association of GRB980425 with supernova SN1998bw (Galama et al. 1998). The clear evidence (Abbott et al. 2017; Mooley et al. 2018; Ghirlanda et al. 2019) in support of the presence of a relativistic jet, observed under a relatively large viewing angle with respect to its axis, in association with the GW170817 BNS merger detected by the Advanced Laser Interferometer Gravitational-wave Observatory (aLIGO, Aasi et al. 2015) and Virgo (Acernese et al. 2014) network and the fact that the inferred characteristics of such jet indicate (e.g. Salafia et al. 2019) that an on-axis observer would have observed an emission consistent with previously known SGRBs, provided the

long-awaited smoking gun of the BNS-SGRB progenitor scenario. Still, the question whether *all* BNS mergers produce a jet (and whether other progenitors contribute a significant fraction of SGRBs) remains open. The answer to this question encodes information about the conditions that lead to the launch of a jet and to its successful propagation up to the location where the observable emission is produced.

The conditions for the launch of a relativistic jet in the immediate aftermath of a BNS merger are set by the jet-launching mechanism, which is not entirely settled: while the Blandford & Znajek (1977) mechanism – which involves the extraction of energy from a spinning black hole by magnetic fields supported by an accretion disc – seems the most favoured one, several authors (e.g. Dai & Lu 1998; Zhang & Mészáros 2001; Metzger et al. 2008; Dall’Osso et al. 2011; Bernardini et al. 2012b,a, 2013; Rowlinson et al. 2013; Gompertz et al. 2013; Stratta et al. 2018; Strang & Melatos 2019; Sarin et al. 2020) invoked a rapidly spinning, highly magnetized neutron star (a proto-magnetar) to explain some observational features such as the so called ‘plateaux’ (Nousek et al. 2006) in early X-ray afterglows and the detection of ‘extended emission’ (Norris & Bonnell 2006) in gamma-rays beyond the usual short-duration prompt emission. On the other hand, many models of the early X-ray afterglow and extended emission do not require a proto-magnetar (e.g. Rees & Mészáros 1998; Zhang et al. 2006; Genet et al. 2007; Yamazaki 2009;

\* The source code behind the manuscript and all the computations is publicly available at <https://>

Leventis et al. 2014; Duffell & MacFadyen 2015; Beniamini et al. 2020; Oganessian et al. 2020; Ascenzi et al. 2020; Barkov et al. 2021; Duque et al. 2021), and the production of a successful jet by such a compact object, while possible (Usov 1992; Thompson 1994; Thompson et al. 2004; Metzger et al. 2011; Mösta et al. 2020), is theoretically disfavoured (e.g. Ciolfi 2020, see also §3.1).

Whether a BNS merger satisfies the jet-launching conditions, whatever they are, depends on the progenitor system parameters and on the equation of state (EoS) of neutron star matter (Fryer et al. 2015; Piro et al. 2017). Indeed, despite their complexity, the merger dynamics are mostly deterministic, so that the properties of the post-merger remnant and any accretion disc are directly linked to the progenitor binary masses and, in principle, spins and magnetic fields. Except for extreme cases, however, pre-merger neutron star spins and magnetic fields are thought to have limited impact (e.g. East et al. 2019; Dudi et al. 2021; Papenfort et al. 2022 for spins; e.g. Giacomazzo et al. 2009; Lira et al. 2022 for magnetic fields). Moreover, the magnetic field in the merger remnant and accretion disc is thought to undergo amplification due to Kelvin-Helmholtz instabilities and dynamo processes (e.g. Kiuchi et al. 2014, 2015; Palenzuela et al. 2021), leading to the loss of memory about the initial magnetization. Therefore, the fraction of jet-launching systems in the BNS merger population is largely determined by the distribution of the progenitor binary masses and by the properties of neutron star matter, that is, by the (not yet well-known) EoS of matter beyond the nuclear saturation density. The incidence of jets in the population therefore carries information about both binary stellar evolution and nuclear physics, which can be investigated especially through multi-messenger observations of these sources.

In principle, a relativistic jet may be launched, but not be able to propagate through the cloud of merger ejecta and break out of it, and some authors suggested (e.g. Moharana & Piran 2017) that this is a frequent outcome. On the other hand, the expected properties of BNS merger ejecta and those of SGRB jets (also in light of GW170817) suggest that the vast majority of jets are successful in breaking out (Duffell et al. 2018; Beniamini et al. 2019; Salafia et al. 2020). In this article, we therefore consider systems that satisfy our ‘jet-launching conditions’ to always lead to a successful jet break out.

In what follows, we derive the posterior probability distributions on the jet incidence, i.e. the fraction of systems that launch a jet, in BNS mergers based on the presence of a jet in GW170817 (§2.1) and on the comparison of local rate densities of SGRBs and BNS mergers (§2.2). We then describe a framework to model the jet incidence under the physically-motivated assumption that launching a jet in the aftermath of the merger requires the collapse of the remnant to a black hole on a short time scale and the presence of a non-negligible accretion disc (§3). Within this framework, we show that knowledge of the jet incidence can be used to constrain the BNS mass distribution and the EoS (§4.1). We show (§4.2) that, within this framework, the currently available information on the jet incidence leads to interesting constraints on the mass distribution, while it does not lead to informative constraints on the EoS. Nevertheless, in §4.3 we show illustrative examples of EoS constraints that can be placed in the future, when the jet incidence will be known with better precision. In Appendix A we show how the methodology can be extended to include multiple events with possibly uncertain jet associations, and in §5 we discuss our results and suggest how this

methodology can be modified to become part of Bayesian hierarchical population studies of BNS mergers.

## 2. Jet incidence from observations

### 2.1. GW-detectable sub-population: binomial argument

Let us call  $f_j$  the fraction of binary neutron star (BNS) mergers in a population that produce a successful relativistic jet. At the time of writing, the only binary neutron star merger detected in GWs whose localisation was sufficiently tight and close-by as to permit a thorough electromagnetic follow-up was GW170817, and a relativistic jet has been clearly detected in association to it (Abbott et al. 2017; Mooley et al. 2018; Ghirlanda et al. 2019). As we show in Appendix A, the poorly constrained sky localisation and larger distance of the other GW-detected BNS merger event (GW190425, Abbott et al. 2020) prevents a useful constraint on the presence or absence of a jet; this event therefore does not carry information about the jet incidence and we ignore it here. Let us model the production of a jet in the GW-detectable BNS subpopulation as a binomial process with single-event success probability  $f_{j,\text{GW}}$ . The probability that a particular set of  $k$  events out of a total of  $n$  mergers produce a successful jet is then given by

$$P(k | n, f_{j,\text{GW}}) = f_{j,\text{GW}}^k (1 - f_{j,\text{GW}})^{n-k}, \quad (1)$$

where the usual binomial coefficient is not present because the events can be distinguished. For a single successful event after a single observation, this is clearly  $P(1 | 1, f_{j,\text{GW}}) = f_{j,\text{GW}}$ . By Bayes’ theorem, the posterior probability density of  $f_{j,\text{GW}}$  is

$$P(f_{j,\text{GW}} | 1, 1) \propto f_{j,\text{GW}} \pi(f_{j,\text{GW}}) \quad (2)$$

where  $\pi(f_{j,\text{GW}})$  is the prior probability density on  $f_{j,\text{GW}}$ . An intuitive and widely adopted choice for an uninformative prior probability is a uniform distribution  $\pi(f_{j,\text{GW}}) = \pi_U = 1$  over the domain of the parameter, which is  $f_{j,\text{GW}} \in [0, 1]$  in our case. A possibly more desirable choice of an uninformative prior is one that is invariant under re-parametrization (Jeffreys 1946). In this particular case, this ‘Jeffreys’ prior reads  $\pi(f_{j,\text{GW}}) = \pi_J(f_{j,\text{GW}}) = f_{j,\text{GW}}^{-1/2} (1 - f_{j,\text{GW}})^{-1/2}$ . With the former choice, the cumulative posterior probability of  $f_{j,\text{GW}}$  is

$$C_U(f_{j,\text{GW}} | 1, 1) = f_{j,\text{GW}}^2 \quad (3)$$

while for the latter choice it takes a slightly more complicated form, namely

$$C_J(f_{j,\text{GW}} | 1, 1) = \frac{2}{\pi} \left[ \arcsin \left( \sqrt{f_{j,\text{GW}}} \right) - \sqrt{f_{j,\text{GW}} - f_{j,\text{GW}}^2} \right]. \quad (4)$$

From the cumulative posterior probability, a lower limit on  $f_{j,\text{GW}}$  at confidence level  $\alpha$  can be derived by solving  $C(f_{j,\text{GW}} | 1, 1) = 1 - \alpha$  for  $f_{j,\text{GW}}$ . In the uniform prior case, this can be done analytically, yielding  $f_{j,\text{GW}} \geq \sqrt{1 - \alpha}$ ; for the Jeffreys prior the lower limit can be obtained numerically, or graphically from Figure 1, which shows a plot of  $C_U$  and  $C_J$ , with the implied 90% confidence lower limit annotated. From this simple argument one can conclude, in agreement

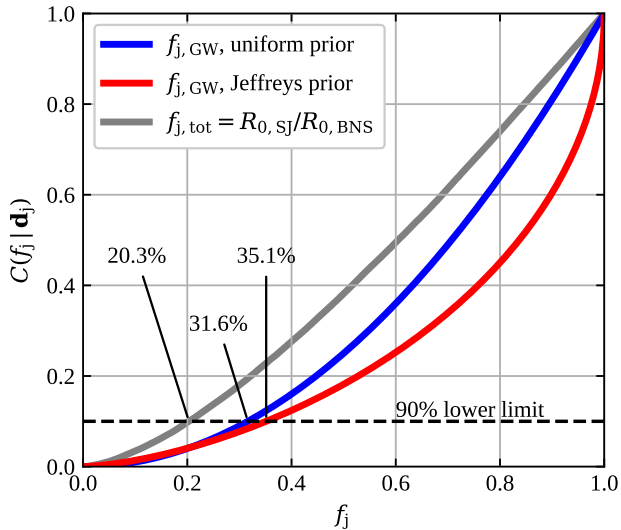


**Fig. 1.** Cumulative posterior probability of the BNS successful jet incidence. The solid red (blue) line refers to the fraction  $f_{j,GW}$  of GW-detectable BNS mergers that produce a successful jet, based on having observed the single successful event GW170817 and adopting the Jeffreys (uniform) prior. The solid grey line refers to the jet incidence  $f_{j,tot}$  in the entire BNS merger population, based on the ratio of the local rate of short GRB jets  $R_{0,SJ}$  to the BNS rate  $R_{0,BNS}$ . The implied 90% credible lower limits are annotated.

with<sup>1</sup> Beniamini et al. (2019) and Ghirlanda et al. (2019), that the relativistic jet in GW170817 implies that a large fraction – at least about one third at the 90% confidence level – of GW-detectable BNS mergers should produce the same outcome, unless we have been extremely lucky in this first case. The corresponding 3-sigma lower limits are 5.2% (3.4%) for the uniform (Jeffreys) prior, showing that a fraction  $f_{j,GW}$  lower than several percent is highly unlikely.

## 2.2. Whole population: SGRB vs BNS local rate

Another route to constraining  $f_j$  is that of comparing the local rate density  $R_{0,SJ}$  of short GRB jets (that is, the beaming-corrected SGRB rate density at  $z = 0$ ) to that of BNS mergers,  $R_{0,BNS}$ . The resulting jet incidence estimate  $f_{j,tot} = R_{0,SJ}/R_{0,BNS}$  then applies to all binaries (in contrast with that obtained in the previous section, which applies to the subpopulation of GW-detectable binaries). In a recent manuscript (Abbott et al. 2021b) describing compact binary merger population analyses including data from the GWTC-3 catalog (Abbott et al. 2021a), the LIGO-Virgo-KAGRA (LVK) Collaboration found local BNS rates in the range  $R_{0,BNS} \in [10 - 1700] \text{ Gpc}^{-3} \text{ yr}^{-1}$  (union of the 90% credible intervals obtained through different analyses), the broad range being partly due to the highly uncertain mass distribution. An independent estimate, based on a larger sample of events, can be made based on known Galactic double neutron stars (Kim et al. 2003). A recent study (Grunthal et al. 2021; see also Pol et al. 2020), which includes observational insights on the beam shape and viewing geometry of the PSRJ1906+0746 pulsar (which contributes significantly to the total rate), finds a Milky

<sup>1</sup> These works provide support for a large  $f_j$  based on the comparison of the single-event rate of GW170817 with the observed short gamma-ray burst rate.

Way BNS merger rate  $\mathcal{R}_{MW} = 32_{-9}^{+19} \text{ Myr}^{-1}$  (maximum *a posteriori* and 90% credible range). Assuming a Milky-Way-Equivalent galaxy density  $\rho_{MWEG} = 0.0116 \pm 0.0035 \text{ Mpc}^{-3}$  in the local Universe (Abadie et al. 2010; Kopparapu et al. 2008, assuming a one-sigma local star formation rate uncertainty of  $\sim 30\%$ , Madau & Fragos 2017), this translates to  $R_{0,BNS} = 390_{-256}^{+303} \text{ Gpc}^{-3} \text{ yr}^{-1}$  (median and 90% credible range, blue line in Fig. 2). In what follows, we will adopt this BNS merger rate estimate as our reference value<sup>2</sup>.

The local SGRB jet rate density is poorly constrained due to the inherent difficulty in disentangling the luminosity function and redshift distribution of the cosmological SGRB population, given the current low number of events with a measured redshift, the complexity of selection effects, and the fact that it is essentially impossible to constrain the low-end of the luminosity function (roughly below  $5 \times 10^{49} \text{ erg/s}$ ). This emerges clearly from the diversity of local rate values present in the literature (Abbott et al. 2021b; Mandel & Broekgaarden 2021; Tan & Yu 2020; Liu & Yu 2019; Sun et al. 2017; Ghirlanda et al. 2016; Wanderman & Piran 2015; Coward et al. 2012). The uncertainty on the beaming-corrected rate density is exacerbated by the difficulty in determining the average beaming factor (and its likely dependence on distance) from the available data. Nevertheless, here we show that a robust lower limit on  $R_{0,SJ}$  can be set based on the single-event rate of GRB170817A, as follows. Let  $V_{\text{eff}}$  be the effective comoving volume over which *Fermi/GBM* is sensitive to an event with the same intrinsic properties as GRB170817A. The rate density  $R_{0,17A}$  that can be derived conservatively assuming GBM to have observed a single SGRB jet in that volume over its entire time of operation  $T = 13 \text{ yr}$ , neglecting any beaming factor, is then a strict lower limit to  $R_{0,SJ}$ . By carefully modelling the GBM sensitive volume based on the peak fluxes of observed short GRBs (as described in Appendix B) we obtain the posterior distribution on  $R_{0,17A}$  shown by the red line in Fig. 2, whose median and 90% credible interval are  $R_{0,17A} = 342_{-337}^{+1800} \text{ Gpc}^{-3} \text{ yr}^{-1}$  (in agreement with e.g. Della Valle et al. 2018). Given this piece of information, our knowledge of  $R_{0,SJ}$  can be modelled as

$$P(R_{0,SJ} | R_{0,17A}) \propto \pi(R_{0,SJ}) \int \Theta(R_{0,SJ} - R_{0,17A}) \pi(R_{0,17A}) dR_{0,17A}, \quad (5)$$

where  $\Theta$  is the Heaviside step function, that is

$$\Theta(x) = \begin{cases} 0 & x < 0 \\ 1 & x \geq 0 \end{cases}. \quad (6)$$

<sup>2</sup> Double neutron star binaries containing an observable pulsar clearly represent only a subpopulation of merging binaries. While Grunthal et al. (2021) carefully account for selection effects and for the pulsar lifetimes in inferring the total number and merger rate of Galactic double neutron stars from the observed population, they do not account for a possible fraction of the population that is not currently detected by radio surveys, which may form through different channels (e.g. Vigna-Gómez et al. 2021) and may account for massive systems such as GW190425 (Abbott et al. 2020). Such systems, on the other hand, are unlikely to constitute a dominant fraction of the total (as also suggested by the relative rate densities of GW170817 and GW190425), and thus the systematic error that stems from using the Grunthal et al. (2021) rate as a proxy for the total BNS rate is most likely less than a factor of 2. The uncertainty in the conversion between the Galactic and local volumetric merger rates incorporated into our analysis may therefore underestimate the total merger rate uncertainty.

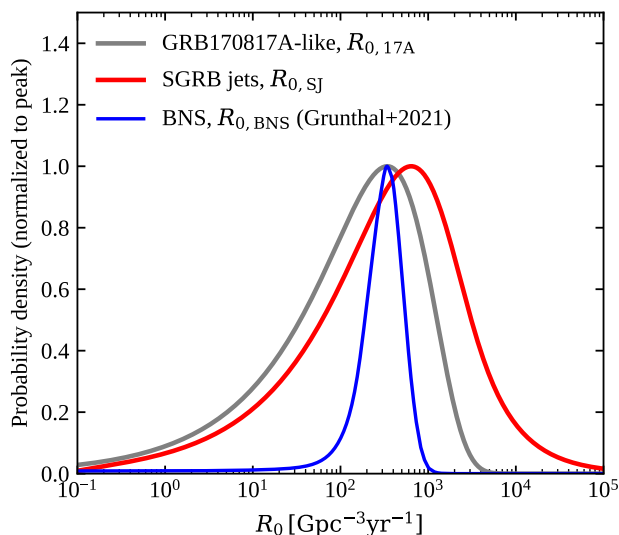


**Fig. 2.** Posterior probability distribution on the local rate density of GRB170817A-like events (grey solid line, Eq. B.1), SGRB jets in general (regardless of orientation, red solid line, Eq. 5), and BNS mergers (as determined from observations of Galactic systems, blue solid line, Grunthal et al. 2021).

We use the above mentioned  $R_{0,17A}$  posterior as our prior  $\pi(R_{0,17A})$ , and adopt a log-uniform prior  $\pi(R_{0,SJ}) \propto R_{0,SJ}^{-1}$  on the SGRB jet rate density, which is a conservative choice as it favours values closer to the lower limit  $R_{0,17A}$ , and hence lower values of  $f_{j,tot}$ . The result is shown in Fig. 2, along with the posterior on  $R_{0,17A}$  and that on  $R_{0,BNS}$  based on Grunthal et al. (2021).

Finally, we compute the  $f_{j,tot}$  posterior distribution as the ratio distribution of the  $R_{0,SJ}$  and  $R_{0,BNS}$  distributions, with the additional constraint  $f_{j,tot} \leq 1$ , namely

$$P(f_{j,tot} | \mathbf{d}_{tot}) \propto \iint dR_{0,SJ} dR_{0,BNS} \delta\left(f_{j,tot} - \frac{R_{0,SJ}}{R_{0,BNS}}\right) \times \Theta(R_{0,BNS} - R_{0,SJ}) P(R_{0,SJ} | R_{0,17A}) \pi(R_{0,BNS}), \quad (7)$$

where  $\delta$  is the Dirac delta function and  $\mathbf{d}_{tot}$  represents the data which inform our estimates of  $R_{0,SJ}$  and  $R_{0,BNS}$  and, hence, the above posterior on  $f_{j,tot}$ . To evaluate Eq. 7 in practice, we produce  $\{f_{j,tot,i}\}_{i=1}^N$  samples by the following procedure: (1) we extract an  $R_{0,SJ,i}$  sample from a log-uniform distribution in the range  $10^{-1} - 10^4 \text{ Gpc}^{-3} \text{ yr}^{-1}$  (that is, a broad enough range as to cover the support of both  $R_{0,17A}$  and  $R_{0,BNS}$ ), and an  $R_{0,17A,i}$  sample from the red distribution in Fig. 2; (2) if  $R_{0,SJ,i} < R_{0,17A,i}$  we go back to (1); (3) we extract an  $R_{0,BNS,i}$  sample from the blue distribution in Fig. 2; (4) if  $f_{j,tot,i} = R_{0,SJ,i}/R_{0,BNS,i} > 1$  we reject the sample and go back to (1), otherwise we store it. The resulting cumulative  $f_{j,tot}$  distribution is shown by the grey line in Figure 1, while two approximations of the probability density are shown in Fig. 3. The implied 90% credible lower limit on  $f_j$  is 21% (2.4% at  $3\sigma$ ). As shown in Fig. 3, the associated probability density is well approximated by a power law

$$P(f_{j,tot} | \mathbf{d}_{tot}) \propto f_{j,tot}^{-\gamma}, \quad (8)$$

with a best fit value  $\gamma = 0.42$ .

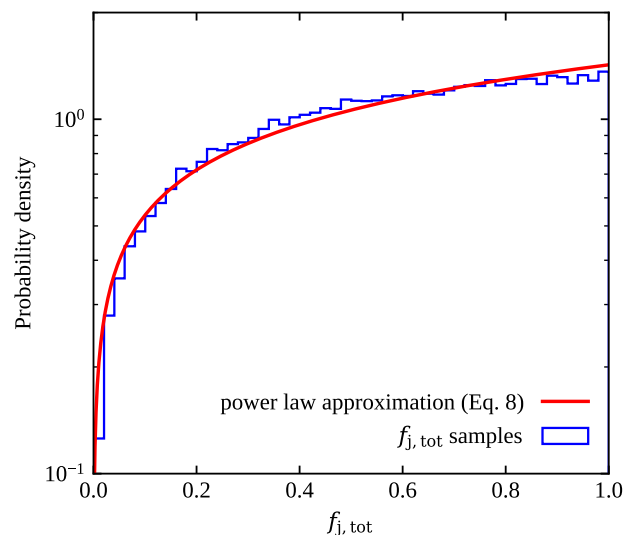


**Fig. 3.** Posterior distribution on the fraction  $f_{j,tot}$  of BNS mergers accompanied by jets, computed as described in §2.2. The blue histogram shows the distribution of samples constructed as described in the text, that approximate Eq. 7, while the red line shows the analytical approximation  $P(f_{j,tot} | \mathbf{d}_{tot}) \propto f_{j,tot}^{-\gamma}$  with  $\gamma = 0.42$ .

We neglect the potential contribution of neutron star - black hole mergers to the beaming-corrected local rate density of SGRB jets. This is justified by the fact that the intrinsic BNS and neutron star - black hole rates are comparable – Abbott et al. 2021a – and most likely only a small fraction of the latter result in the tidal disruption of the neutron star, given the expected dearth of rapidly spinning BHs in these systems (see e.g. Broekgaarden et al. 2021 and Zappa et al. 2019). Other works take the alternative route of constraining the beaming factor (or the angular dependence of the jet emission properties) from the comparison of the observed rates of BNS mergers and SGRBs (e.g. Williams et al. 2018; Biscoveanu et al. 2020; Farah et al. 2020; Hayes et al. 2020), or of estimating the future joint BNS-SGRB detection rates as a function of such factor (e.g. Chen & Holz 2013; Clark et al. 2015).

## 3. Modelling the jet incidence

### 3.1. Blandford-Znajek jet launching conditions

The gamma-ray burst jet launching mechanism is still under debate (see Salafia & Giacomazzo 2021 for a recent discussion and Kumar & Zhang 2015 for a review). In the case of a binary neutron star merger progenitor, the possible mechanisms are restricted to those compatible with the characteristics of the merger remnant: depending on the component neutron star masses and equation of state, the merger can lead either to the prompt formation (i.e. happening on a dynamical timescale) of a black hole (BH) or to a proto-neutron star (Burrows & Lattimer 1986). If the mass  $M_{rem}$  of the latter is below the maximum mass  $M_{TOV}$  that can be supported against collapse in a non-rotating neutron star, it will evolve to an indefinitely stable neutron star (NS); if the mass is above  $M_{TOV}$ , but below the mass  $M_{max,rot}$  that can be supported by uniform rotation at the mass-shedding limit (Goussard et al. 1997), the remnant is said to be a ‘supra-massive’ neutron star (SMNS) and it can survive until electromagnetic spin-down eventually

leads to collapse to a BH; if  $M_{\text{rem}} > M_{\text{max,rot}}$ , the proto-neutron star can still be supported (Goussard et al. 1998) for a short time (typically  $\lesssim 100$  ms) by differential rotation before collapsing, in which case it is termed a ‘hyper-massive’ neutron star (HMNS).

Jets launched by neutron stars are observed in our Galaxy (e.g. Pavan et al. 2014; van den Eijnden et al. 2018) and several authors have argued that a rapidly spinning, highly magnetized proto-neutron star merger remnant may be able to launch a relativistic jet (e.g. Usov 1992; Thompson 1994; Thompson et al. 2004; Metzger et al. 2011; Mösta et al. 2020). On the other hand, the neutrino-driven (Dessart et al. 2009; Perego et al. 2014) and magnetically-driven (Ciolfi & Kalinani 2020) winds produced by a proto-neutron star during its early evolution are likely to load the surrounding environment with too many baryons, preventing a putative jet from reaching relativistic speeds (e.g. Ciolfi 2020).

If the remnant is a BH (or it collapses to a BH in a time much shorter than the accretion time scale), following the amplification of the magnetic field by Kelvin-Helmholtz instabilities triggered at merger (Obergaullinger et al. 2010; Kiuchi et al. 2015; Aguilera-Miret et al. 2020) and the development of a large-scale ordered magnetic field configuration with a non-negligible poloidal component, the Blandford-Znajek jet-launching mechanism (Blandford & Znajek 1977; Komissarov 2001; Tchekhovskoy et al. 2010) can operate, possibly enhanced by energy deposition from the annihilation of neutrino-antineutrino pairs emitted by the inner accretion disc (Eichler et al. 1989 – even though this cannot be the dominant source of jet power, as found by Just et al. 2016).

Given the difficulties with the proto-neutron star central engine, in this work we assume that only a BH remnant (possibly, but not necessarily, formed after a HMNS phase) can launch a relativistic jet. Very broadly speaking, the conditions for the Blandford-Znajek mechanism to operate are the presence of a spinning black hole (BH), an accretion disc with a large-scale ordered magnetic field, and a low-density funnel above the BH (along its rotation axis). Given the particular accretion conditions in the BNS post-merger phase and the expected predominantly toroidal configuration of the magnetic field in the disc (Kiuchi et al. 2014; Kawamura et al. 2016), the accretion-to-jet energy conversion efficiency  $\eta = E_{\text{jet}}/(M_{\text{disc}}c^2)$  of the Blandford-Znajek mechanism in these systems (Christie et al. 2019) is likely quite low,  $\eta \sim 10^{-3}$ , as found in numerical relativity simulations (Ruiz et al. 2018) and in agreement with the estimate that can be made based on GW170817 (Salafia & Giacomazzo 2021). Assuming this efficiency, in order to produce a (short) gamma-ray burst jet with a total energy in the typical (Fong et al. 2015) range  $E_{\text{jet}} \sim 10^{49} - 10^{50}$  erg, a disc mass of about  $M_{\text{disc}} \sim 0.01 - 0.1 M_{\odot}$  is needed.

Based on these arguments, we assume GRB jet launching to be possible only for HMNS or prompt BH remnants<sup>3</sup>, provided that the accretion disc mass is, conservatively<sup>4</sup>, at least  $M_{\text{disc,min}} = 10^{-3} M_{\odot}$ . The first condition can be re-

<sup>3</sup> We note that the inclusion of prompt BH collapse cases is justified by the fact that sufficiently asymmetric systems can produce massive accretion discs by the tidal disruption of the secondary neutron star, regardless of the nature of the remnant (Bernuzzi et al. 2020).

<sup>4</sup> We note that changing this to a more stringent value, e.g.  $M_{\text{disc,min}} = 10^{-2} M_{\odot}$ , would have a very limited impact on our results due to the steep dependence of the disc mass on the gravitational mass  $M_2$  of the secondary component in the binary (Krüger & Foucart 2020), as demonstrated in Figure 4. For the same reason,

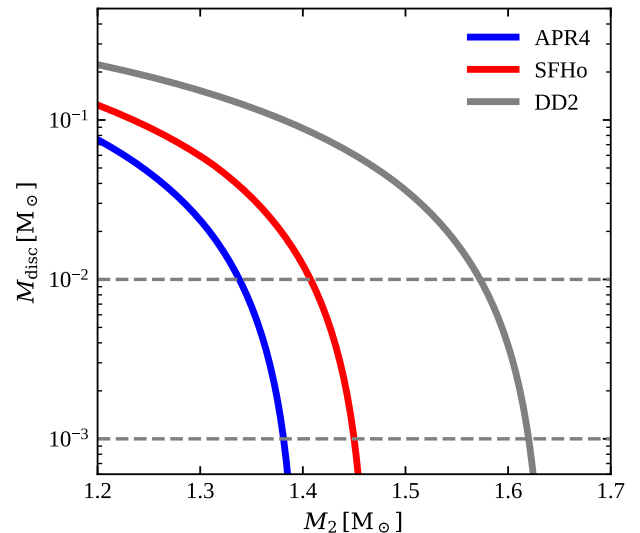


**Fig. 4.** Dependence of the disc mass on the mass of the secondary component in the binary, according to the fitting formula by Krüger & Foucart (2020). Different colors refer to different assumed equations of state, as shown in the legend.

stated as the requirement that the gravitational mass  $M_{\text{rem}}$  of the merger remnant be at least as massive as the maximum mass that can be supported by uniform rotation  $M_{\text{max,rot}} = 1.2M_{\text{TOV}}$ , where  $M_{\text{TOV}}$  is set by the chosen neutron star matter equation of state (EoS) and the factor 1.2 is essentially EoS-independent<sup>5</sup> (Breu & Rezzolla 2016).

### 3.2. Determination of the remnant type

In order to compute the remnant mass  $M_{\text{rem}}$ , we invoke energy conservation for a merging binary with total mass  $M = M_1 + M_2$ , equating the energy budget of the initial state (at formally infinite binary separation) to that of the final state after the remnant has formed, in the form

$$Mc^2 = M_{\text{rem}}c^2 + E_{\text{GW}} + E_{\text{disc}} + E_{\text{ej}} + E_{\nu}, \quad (9)$$

where  $E_{\text{GW}}$  is the energy radiated in gravitational waves,  $E_{\text{disc}}$  is the total energy associated to the accretion disc and  $E_{\text{ej}}$  is that associated to the ejecta (except for disc winds, which are included in  $E_{\text{disc}}$ ), and  $E_{\nu}$  is the energy lost in neutrinos by the remnant (in the absence of a prompt BH collapse). We compute  $E_{\text{GW}}$  using numerical-relativity-based fitting formulae from Zappa et al. (2018), which include GW mass loss all the way from the inspiral to the early post-merger phase, and are implemented in the publicly available repository `bns_lum` (Bernuzzi et al. 2018). The disc energy in principle comprises its rest-mass, its gravitational potential energy, the energy associated to its rotation and that contained in the magnetic field: the rotational and gravitational potential energy together amount approximately to  $-GM_{\text{rem}}M_{\text{disc}}/2R_{\text{disc}} = -(R_{\text{g,rem}}/R_{\text{disc}})M_{\text{disc}}c^2/2$  (where  $R_{\text{g,rem}}$  and  $R_{\text{disc}}$  are the remnant gravitational radius and the disc radius, respectively). Since very generally

the uncertainty in the disc mass fitting formula has little impact on our results.

<sup>5</sup> A small deviation from this quasi-universal value is expected for equations of state with a first-order phase transition (e.g. Bozzola et al. 2019).

$R_{\text{disc}} \gg R_{\text{g,rem}}$ , these terms can be safely neglected. As stated in the previous section, during the merger the magnetic field is amplified by Kelvin-Helmholtz instabilities, reaching typical energies of  $\sim 10^{51}$  erg (Aguilera-Miret et al. 2020). This is equivalent to less than 0.1% of a solar mass, so that this term can also be neglected. Therefore, we keep only the rest-mass contribution, that is  $E_{\text{disc}} \sim M_{\text{disc}}c^2$ . We compute the disc rest-mass  $M_{\text{disc}}$  using the fitting formula proposed in (Krüger & Foucart 2020, their eq. 4, with their best-fit parameters, to which we refer hereafter as  $M_{\text{disc,KF20}}$ ). Similarly, since the typical neutron star merger ejecta velocities are subrelativistic,  $v_{\text{ej}} \sim 0.1 - 0.2c$ , we neglect their kinetic energy and we write  $E_{\text{ej}} \sim M_{\text{ej}}c^2$ . The mass  $M_{\text{ej}}$  includes the dynamical ejecta, which we compute through the relevant fitting formula from (Krüger & Foucart 2020, their eq. 6, with their best-fit coefficients), and potentially also winds from a long-lived neutron star remnant. The typical mass of neutrino-driven winds from a HMNS is expected (Dessart et al. 2009; Perego et al. 2014) to be on the order of  $10^{-4} M_{\odot}$  and can be safely neglected in our treatment; winds driven by magnetically-induced viscosity can be much more substantial, reaching  $\sim 10^{-2} M_{\odot}$  (Ciolfi & Kalinani 2020) in sufficiently long-lived cases, but this is still well within the expected uncertainty of the fitting formula we employ for the disc mass (Krüger & Foucart 2020), and therefore we do not include this component for simplicity. Similarly, since the peak neutrino luminosity of an HMNS remnant is expected to be below  $L_{\nu} < 10^{53}$  erg/s (Dessart et al. 2009; Perego et al. 2014), and the HMNS lifetime (which is of the order of the viscous timescale in the HMNS, since differential rotation is damped by viscous angular momentum transport, e.g. Kiuchi et al. 2018) is  $t_{\text{HMNS}} \lesssim 0.1$  s, the mass lost in neutrinos  $M_{\nu} = E_{\nu}/c^2 \sim L_{\nu}t_{\text{HMNS}}/c^2$  is well below one percent of a solar mass, and thus we set  $E_{\nu} = 0$ .

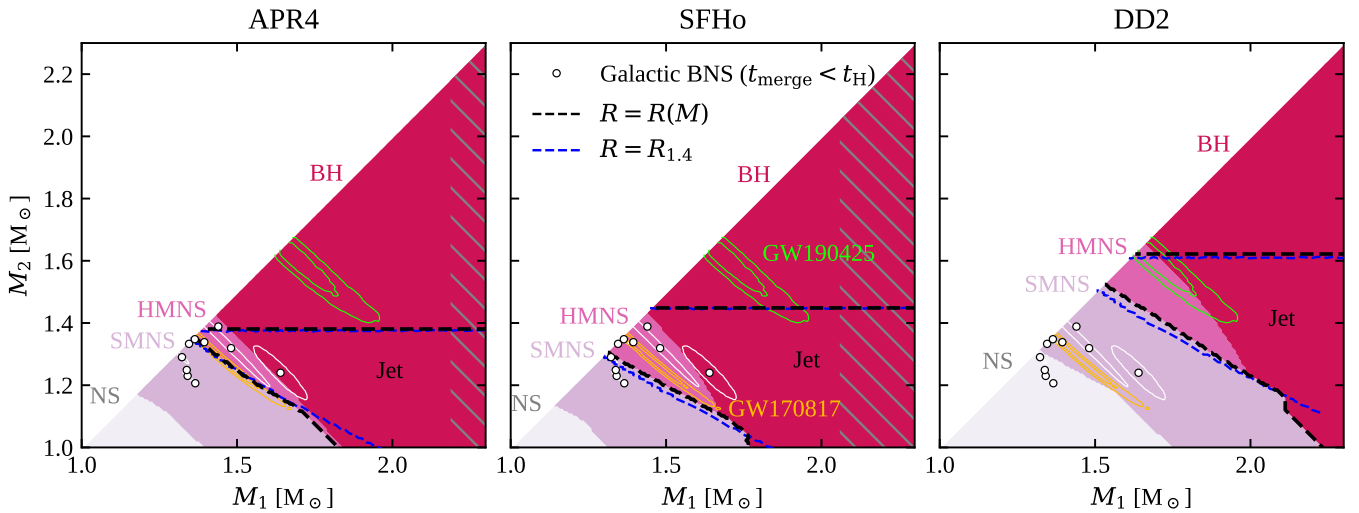
The employed fitting formulae depend on the neutron star masses and on their compactness or dimensionless tidal deformability: if an EoS is assumed, the neutron star radii can be computed from the mass-radius relation, and the tidal deformabilities from the ‘C-Love’ universal relation (Yagi & Yunes 2017). This allows one to solve Eq. 9 for  $M_{\text{rem}} = M_{\text{rem}}(M_1, M_2, \theta_{\text{EoS}})$ , where  $\theta_{\text{EoS}}$  represents a set of parameters that define the EoS. Setting  $M_{\text{rem}} < M_{\text{TOV}}$  as the condition for an indefinitely stable NS remnant;  $M_{\text{TOV}} \leq M_{\text{rem}} < 1.2M_{\text{TOV}}$  as the condition for a SMNS remnant;  $1.2M_{\text{TOV}} \leq M_{\text{rem}} < M_{\text{thresh}}$  as the condition for a HMNS remnant, and  $M_{\text{rem}} \geq M_{\text{thresh}}$  for direct collapse to a BH, one can then determine the fate of the merger remnant based on the initial binary masses and on the EoS. Here  $M_{\text{thresh}}$  is the threshold mass for BH direct collapse, which can be computed employing the mass ratio-dependent fitting formula given in Bauswein et al. 2021. Alternative recent formulae exist (e.g. Tootle et al. 2021; Kashyap et al. 2021; Kölsch et al. 2021), but we note that our results do not depend on this choice: the  $M_{\text{thresh}}$  line shown in Fig. 5 as the separation between the HMNS and BH remnant regions is only illustrative and it does not enter our assumed jet-launching conditions.

Figure 5 shows the resulting regions that correspond to different expected remnants of BNS mergers on the  $(M_1, M_2)$  plane, assuming three different EoSs, namely APR4 (Akmal et al. 1998), SFHo and DD2 (Hempel et al. 2012), which predict maximum masses  $M_{\text{TOV}}/M_{\odot} = 2.19, 2.06$  and  $2.42$ , respectively (all of which are above the largest Galactic neutron star masses measured to date, Lynch et al. 2013; Fonseca et al. 2021), and radii in the range  $R_{1.4} \in (11.30, 13.25)$  km

for a  $1.4 M_{\odot}$  neutron star, in agreement with constraints from GW170817 (Abbott et al. 2018, 2019) and from NICER (Miller et al. 2019; Raaijmakers et al. 2019, 2020; Landry et al. 2020, with some tension in the case of DD2). The black dashed lines enclose the region where our GRB jet launching conditions are met. The upper boundary is a horizontal line: this is due to the fact that the disc mass fitting formula by Krüger & Foucart (2020) depends only on the compactness of the least massive neutron star, but we verified that a weak dependence on the mass of the most massive NS is reflected in other recent disc mass fitting formulae (Dietrich et al. 2020; Barbieri et al. 2021), which also lead to upper boundaries that are close to horizontal. The blue dashed lines show the result obtained by adopting the simplified EoS dependence described in the next section, plugging in the  $M_{\text{TOV}}$  and  $R_{1.4}$  values implied by each EoS. Confidence contours for the component masses of GW170817 (Abbott et al. 2019) and GW190425 (Abbott et al. 2020) are shown for reference. For the two softer equations of state, APR4 and SFHo, our jet-launching conditions are most likely satisfied in GW170817 and also in a significant fraction of Galactic BNS (4/10 for APR4; 6/10 for SFHo). If the stiffer DD2 EoS is adopted, then GW170817 clearly falls in the supra-massive neutron remnant region: if such an EoS were found to best represent neutron star matter, then the jet-launching mechanism that operated in the case of GW170817 would have to be something different from Blandford-Znajek.

### 3.3. Approximate two-parameter EoS dependence

Our assumed jet-launching conditions require, in practice, the merger remnant mass to satisfy  $M_{\text{rem}} > 1.2M_{\text{TOV}}$  and the disc mass to satisfy  $M_{\text{disc}} > M_{\text{disc,min}}$ . A rough idea of where the former separation line stands can be obtained by writing a simplified remnant mass equation  $M_{\text{rem}} \sim M - E_{\text{GW}}/c^2 - M_{\text{disc}}$ , thus neglecting the dynamical ejecta mass (in addition to all other terms which we already neglect for the reasons explained in the previous section). This leads to a critical total mass for jet launch  $M_{\text{crit}} \sim (1.2M_{\text{TOV}} + M_{\text{disc}})/(1 - \eta_{\text{GW}})$ , where  $\eta_{\text{GW}} = E_{\text{GW}}/(Mc^2)$ . This places the critical mass in the range  $M_{\text{crit}}/M_{\odot} \in [2.4, 3.26]$  for  $2 \leq M_{\text{TOV}}/M_{\odot} \leq 2.5$ ,  $M_{\text{disc}} \leq 0.1M_{\odot}$  and  $\eta_{\text{GW}} \leq 0.05$ . Assuming equal masses, the component masses are therefore in the range  $M_{1,2}/M_{\odot} \in [1.2, 1.63]$ . For most viable EoSs, the NS radius is approximately constant within this mass range (e.g. Özel & Freire 2016), so that one can quite safely assume it to be equal to  $R_{1.4}$ , i.e. that of a reference  $1.4 M_{\odot}$  NS. Fixing the NS radius to this value, the compactness of the secondary can be determined from its mass. The disc mass computed using the  $M_{\text{disc,KF20}}$  fitting formula thus becomes a function of  $M_2$  only. A reasonable estimate of  $\eta_{\text{GW}}$  can be obtained as the absolute value of the Keplerian orbital energy of two point masses  $(M_1, M_2)$ , at a  $2R_{1.4}$  separation, divided by  $Mc^2$ , which gives  $\eta_{\text{GW}} \sim \nu GM/4R_{1.4}c^2$ , where  $\nu = M_1M_2/M^2 = (2 + q + q^{-1})^{-1}$  is the symmetric mass ratio. This effectively reduces the EoS dependence of  $M_{\text{crit}}$  to only two parameters, namely  $\theta_{\text{EoS}} = \{R_{1.4}, M_{\text{TOV}}\}$ . In Figure 5 we show the  $M_{\text{crit}}$  obtained with this method (oblique blue dashed lines). To obtain also the line beyond which  $M_{\text{disc}} < 10^{-3} M_{\odot}$  (horizontal blue dashed lines), we employed the  $M_{\text{disc,KF20}}$  fitting formula keeping the NS radius fixed at  $R_{1.4}$ . These examples show that the approximate method yields results that differ from the more accurate ones (black dashed lines) at the percent level. In the remainder of



**Fig. 5.** Merger remnant and GRB launching regions on the component mass plane. The filled coloured regions correspond to different BNS merger remnants on the  $(M_1, M_2)$  plane, assuming different EoSs: APR4 (left-hand panel), SFHo (central panel) and DD2 (right-hand panel). Grey hatches mark masses that are above the maximum non-rotating mass supported by the EoS. The black dashed lines enclose the region where our GRB jet launching conditions are met, computed as described in §3.1 (the blue dashed lines, shown for comparison, are computed with the approximate method described in §3.3). White circles and contours show the best fit and 90% credible contours of masses of known Galactic BNS systems whose coalescence time  $t_{\text{merge}}$  is shorter than a Hubble time ( $t_H$ , data from Farrow et al. 2019). The orange and green contours show the 50% and 90% credible regions for the component masses in GW170817 (Abbott et al. 2019) and GW190425 (Abbott et al. 2020), respectively, adopting low-spin priors.

this work, we adopt the simplified 2-parameter dependence described above.

### 3.4. EoS priors and jet probability on the $(M_1, M_2)$ plane

In our framework, the currently available information on the EoS needs to be expressed in the form of priors on  $R_{1.4}$  and  $M_{\text{TOV}}$ . For both quantities there exists a variety of recent constraints that use either electromagnetic or GW information, or try to combine both.

The very thorough and complete recent work by Miller et al. (2021) based on X-ray pulsar radius measurements from NICER and XMM-Newton combined with GW constraints found  $R_{1.4} = 12.45 \pm 0.65$  km (one sigma) consistently using three independent frameworks, showing that the result is robust against systematics. We will therefore use a normal distribution with mean 12.45 km and standard deviation 0.65 km as our prior on  $R_{1.4}$ .

The available constraints on  $M_{\text{TOV}}$  are more uncertain and model-dependent, as can be partly appreciated by looking at the posteriors on  $M_{\text{TOV}}$  reported in Fig. 6, which have been obtained in recent works by three different groups using four different frameworks. On the other hand, a model-independent constraint is set by the mass of the heaviest known pulsar<sup>6</sup> PSRJ0740+6620 (Cromartie et al. 2020), whose measurement has been recently refined (Fonseca et al. 2021) to  $M_{\text{PSR}} = 2.08 \pm 0.07 M_{\odot}$  based on high-cadence data from the Green Bank Telescope (GBT) and the Canadian Hydrogen Intensity

<sup>6</sup> The PSRJ0740+6620 pulsar is inferred to spin at a frequency of roughly 350 Hz (Cromartie et al. 2020), which is up to 25% of the Keplerian (i.e. mass shedding) frequency for viable EoSs (see Haensel et al. 2009). Rotation at such a rate increases the maximum mass that can be supported by the EoS by up to 0.85% (Breu & Rezzolla 2016). We neglect this small correction here, as it is well below our uncertainties.

Mapping Experiment (CHIME). Moreover, the observation of a jet in GW170817 implies, according to our jet-launching conditions, that the remnant gravitational mass  $M_{\text{rem,GW17}}$  was above  $1.2M_{\text{TOV}}$ . Within our framework, after fixing  $R_{1.4}$  we can compute the posterior probability on  $M_{\text{rem,GW17}}$  using the procedure described in §3.2 and the publicly available posterior samples on the GW170817 component masses (Abbott et al. 2019, where we conservatively adopted the samples from the high-spin prior analysis, which yield broader posteriors). Then, the conditions  $M_{\text{TOV}} > M_{\text{PSR}}$  and  $1.2M_{\text{TOV}} < M_{\text{rem,GW17}}$  lead to a prior on  $M_{\text{TOV}}$  conditioned on a particular value of  $R_{1.4}$  that can be expressed as

$$\pi(M_{\text{TOV}} | R_{1.4}, \xi_d) \propto \Phi_{M_{\text{PSR}}}(M_{\text{TOV}}) [1 - \Phi_{M_{\text{rem,GW17}}}(1.2M_{\text{TOV}})], \quad (10)$$

where  $\Phi_x(m)$  represents the cumulative posterior distribution of  $x$  evaluated at  $m$ . To account for the uncertainty in the disc mass fitting formula, we introduced in the above formulation an additional nuisance parameter  $\xi_d$ , so that  $M_{\text{disc}}(M_2, R_{1.4}, \xi_d) = \xi_d M_{\text{disc,KF20}}(M_2, R_{1.4})$ . The prior on this parameter is defined to reflect the 50% uncertainty in the disc mass fitting formula as estimated by Krüger & Foucart (2020), that is

$$\pi(\xi_d) \propto \mathcal{N}_{1,0.5}(\xi_d) \Theta(\xi_d), \quad (11)$$

where

$$\mathcal{N}_{\mu,\sigma}(x) \propto \exp \left[ -\frac{1}{2} \left( \frac{x - \mu}{\sigma} \right)^2 \right]. \quad (12)$$

The joint prior on  $M_{\text{TOV}}$ ,  $R_{1.4}$  and  $\xi_d$  is therefore

$$\pi(M_{\text{TOV}}, R_{1.4}, \xi_d) = \pi(R_{1.4}) \pi(\xi_d) \pi(M_{\text{TOV}} | R_{1.4}, \xi_d), \quad (13)$$

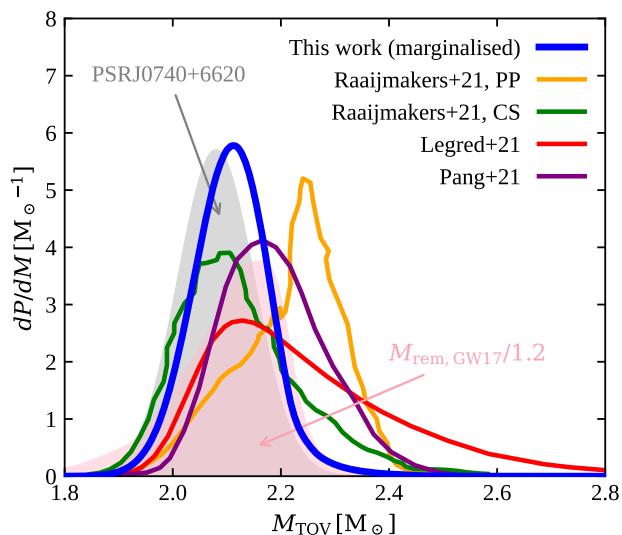


**Fig. 6.** Our prior on  $M_{\text{TOV}}$  compared to recent model-dependent constraints in the literature. The blue thick line shows the marginalised  $M_{\text{TOV}}$  prior we adopt in this work, which is constructed using the latest PSRJ0740+6620 mass measurement (Fonseca et al. 2021, grey filled area) as a lower limit and the remnant mass of GW170817 divided by 1.2 (pink filled area) as an upper limit (see text for an explanation). The remaining lines show results that combine multi-messenger constraints within different frameworks: the orange and green lines show the results obtained by Raaijmakers et al. (2021a) adopting their piecewise-polytropic (PP) and sound-speed (CS) parametrized EoS models, respectively; the dark red line shows the result from Legred et al. (2021) based on a non-parametric, Gaussian-processes-based EoS model; the purple line shows the result from Pang et al. (2021), who adopt an EoS model informed by chiral effective field theory.

where

$$\pi(R_{1.4}) = \mathcal{N}_{12.45, 0.65} \left( \frac{R_{1.4}}{\text{km}} \right) \quad (14)$$

as explained above.

Figure 6 shows the marginalised prior on  $M_{\text{TOV}}$ , that is, Eq. 13 marginalised over  $R_{1.4}$  and  $\xi_d$  (thick blue solid line), compared to recent multi-messenger constraints on  $M_{\text{TOV}}$  from the literature. The comparison shows that our prior on  $M_{\text{TOV}}$  is compatible with other recent works in the literature, but with less support at high masses in most cases, as a consequence of the assumption on the GW170817 remnant. We note that similar results based on analogous arguments have been presented by, e.g., Rezzolla et al. (2018), Shibata et al. (2019) and Annala et al. (2022).

Using the above-defined joint prior, we can compute the probability that a  $M_1, M_2$  binary satisfies our jet launching conditions as

$$P_j(M_1, M_2) = \iiint \Theta_j \pi(M_{\text{TOV}}, R_{1.4}, \xi_d) dM_{\text{TOV}} dR_{1.4} d\xi_d \quad (15)$$

where  $\Theta_j(M_1, M_2, \theta_{\text{EoS}}) = 1$  if our jet launching conditions are met, and  $\Theta_j = 0$  otherwise. More explicitly,

$$\Theta_j = \Theta(M_{\text{rem}} - 1.2M_{\text{TOV}})\Theta(M_{\text{disc}} - M_{\text{disc, min}}), \quad (16)$$

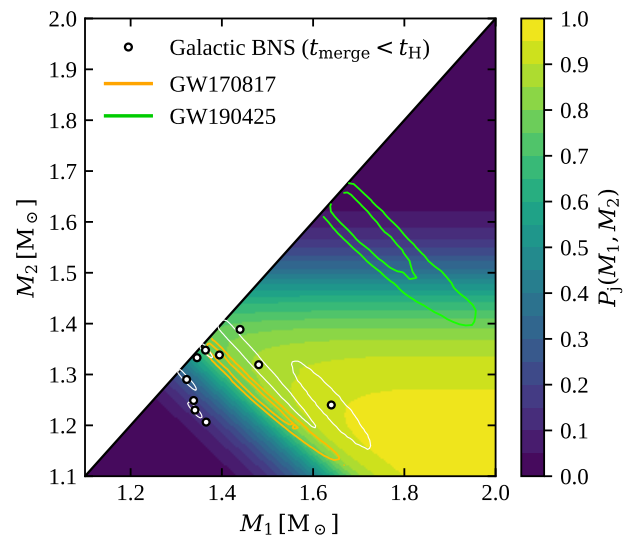


**Fig. 7.** Probability that a BNS would satisfy our jet launching conditions (Eq. 15) as a function of the component masses  $M_1$  and  $M_2$ , given our present knowledge of the EoS (encoded in the priors defined in §3.4). The masses of Galactic BNS systems that merge within a Hubble time and the two GW-detected BNS are shown for comparison, in the same way as in Fig. 5.

where we stress that  $M_{\text{rem}}$  and  $M_{\text{disc}}$  depend on the merging binary component masses, the EoS and the nuisance parameter  $\xi_d$ . The result of Eq. 15 for our choice of EoS priors is shown in Figure 7. The lighter the colour, the more likely our jet launching conditions are met, given our present knowledge about the EoS<sup>7</sup>. For systems located in the dark lower-left corner of the plot, we can confidently predict that their remnant will not collapse to a black hole on a short timescale, preventing the Blandford-Znajek mechanism from operating. Jet-launching by the same mechanism is also confidently excluded for systems in the upper-right dark corner, as these produce negligible accretion discs. The  $f_{j, \text{tot}}$  (or  $f_{j, \text{GW}}$ ) lower limits from section 2 therefore lead qualitatively to the conclusion that *we can exclude that the large majority (indicatively more than 90%) of BNS systems are located in the darkest regions of this plot*. The absence of observed BNS mergers or Galactic double neutron stars in these regions is therefore not due to selection effects, and models that predict a large fraction of low-mass systems, such as many population synthesis models (e.g. Fryer et al. 2012; Dominik et al. 2012; Vigna-Gómez et al. 2018; Mapelli & Giacobbo 2018), are therefore in clear tension with these results.

<sup>7</sup> We note that the value of  $P_j$  averaged over the GW170817 joint component mass posterior (adopting the low-spin-prior samples from Abbott et al. 2019) is 78%. This is not 100% because the information that GW170817 successfully launched a jet enters only through the prior on  $M_{\text{TOV}}$  and it cannot be applied self-consistently to the GW170817 masses within the present method. An alternative approach that solves this issue is outlined in the discussion section.



## 4. Inference on the BNS mass distribution and the EoS based on the jet incidence

### 4.1. Derivation

Our jet launching conditions depend on the component masses  $M_1$ ,  $M_2$  and on the EoS through  $M_{\text{TOV}}$  and the dependence of the disc mass on the compactness of the secondary neutron star. For a fixed mass distribution  $d^2P/dM_1dM_2$  of BNS mergers and EoS, one can compute  $f_{j,\text{tot}}$  directly from

$$\tilde{f}_{j,\text{tot}} = \iint \frac{d^2P}{dM_1dM_2} \Theta_j dM_1 dM_2, \quad (17)$$

where we use the tilde ( $\tilde{\cdot}$ ) to distinguish this functional (which depends on the mass distribution and on the EoS) from the  $f_{j,\text{tot}}$  observable. Similarly, one could compute the jet incidence in GW-detected binaries as

$$\tilde{f}_{j,\text{GW}} = \frac{\iint V_{\text{eff}} \frac{d^2P}{dM_1dM_2} \Theta_j dM_1 dM_2}{\iint V_{\text{eff}} \frac{d^2P}{dM_1dM_2} dM_1 dM_2}, \quad (18)$$

where  $V_{\text{eff}}$  represents the GW detector sensitive volume for a binary with masses  $M_1$  and  $M_2$ , averaged over all extrinsic parameters. For the present detector network, whose BNS range is bound to  $z \ll 1$  and whose SNR is dominated by the inspiral phase, a good approximation is  $V_{\text{eff}} \propto M_c^{5/2}$ , where  $M_c = (M_1 M_2)^{3/5} / (M_1 + M_2)^{1/5}$  is the chirp mass (e.g. Mandel et al. 2019). In what follows, we will use  $f_j$  to indicate either  $f_{j,\text{tot}}$  or  $f_{j,\text{GW}}$  (depending on which one of the constraints shown in Fig. 1 is used), and  $\tilde{f}_j$  to indicate  $\tilde{f}_{j,\text{tot}}$  or  $\tilde{f}_{j,\text{GW}}$  accordingly; we will also use  $\mathbf{d}$  to indicate the data that is used to constrain  $f_j$ , that is the information on the jet incidence in GW-detected BNS binaries (§2.1, i.e. the fact that GW170817 launched a jet, which we denote hereon by  $\mathbf{d}_{\text{GW}}$ ) or that on the SGRB and BNS local rate densities (§2.2, i.e.  $\mathbf{d}_{\text{tot}}$ ). Expressing the mass distribution in a parametric form with a set of parameters  $\theta_{\text{m}}$ , and again the EoS with a set of parameters  $\theta_{\text{EoS}}$  (we include in this set, for ease of presentation, also the nuisance parameter  $\xi_{\text{d}}$ ), we can formally use Bayes' theorem to infer posteriors on these parameters from  $f_j$ , obtaining

$$P(\theta_{\text{m}}, \theta_{\text{EoS}} | f_j) \propto P(f_j | \theta_{\text{m}}, \theta_{\text{EoS}}) \pi(\theta_{\text{m}}, \theta_{\text{EoS}}), \quad (19)$$

where  $\pi(\theta_{\text{m}}, \theta_{\text{EoS}})$  is the prior<sup>8</sup> on  $\theta_{\text{m}}$  and  $\theta_{\text{EoS}}$ , and the likelihood term is simply

$$P(f_j | \theta_{\text{m}}, \theta_{\text{EoS}}) = \delta(f_j - \tilde{f}_j(\theta_{\text{m}}, \theta_{\text{EoS}})). \quad (20)$$

Since the latter is not known exactly, but it is in turn inferred from  $\mathbf{d}$ , we have

$$P(\theta_{\text{m}}, \theta_{\text{EoS}} | \mathbf{d}) = \int_0^1 P(\theta_{\text{m}}, \theta_{\text{EoS}} | f) P(f_j | \mathbf{d}) df_j, \quad (21)$$

which, using Eq. 20, simplifies to

$$P(\theta_{\text{m}}, \theta_{\text{EoS}} | \mathbf{d}) \propto P(f_j = \tilde{f}_j(\theta_{\text{m}}, \theta_{\text{EoS}}) | \mathbf{d}) \pi(\theta_{\text{m}}, \theta_{\text{EoS}}). \quad (22)$$

<sup>8</sup> The priors on  $\theta_{\text{m}}$  and  $\theta_{\text{EoS}}$  are not necessarily independent from each other, as the mass distribution parameters can for example include  $M_{\text{TOV}}$ .

This equation expresses the joint constraint on the EoS and mass distribution parameter space that can be set by our arguments. For current constraints, using equations 2 and 8 and conservatively adopting a uniform prior on  $f_j$ , this can be finally written as

$$P(\theta_{\text{m}}, \theta_{\text{EoS}} | \mathbf{d}) \propto [\tilde{f}_j(\theta_{\text{m}}, \theta_{\text{EoS}})]^\gamma \pi(\theta_{\text{m}}, \theta_{\text{EoS}}). \quad (23)$$

where  $\gamma = 1$  if  $f_j = f_{j,\text{GW}}$  (see §2.1) or  $\gamma = 0.42$  if  $f_j = f_{j,\text{tot}}$  (see §2.2). The somewhat shallower constraint on  $f_{j,\text{tot}}$  with respect to  $f_{j,\text{GW}}$  is partly compensated by the  $V_{\text{eff}}$  term in Eq. 18 but, as we show in the following section, the  $f_{j,\text{GW}}$  is still the most constraining one between the two, given the currently available data.

### 4.2. Mass distribution constraints

The formalism derived in the previous section can be used to investigate the parameter space of a mass distribution model. Given our a priori knowledge of the EoS, encoded in the prior, we can marginalise Eq. 23 over  $\theta_{\text{EoS}}$  to formally obtain the posterior on the mass distribution parameters, namely

$$P(\theta_{\text{m}} | \mathbf{d}) \propto \int \tilde{f}_j^\gamma \pi(\theta_{\text{EoS}}, \theta_{\text{m}}) d\theta_{\text{EoS}}. \quad (24)$$

Taking a uniform prior on the mass distribution parameters,  $\pi(\theta_{\text{m}}) \propto 1$ , this essentially reduces to averaging  $\tilde{f}_j^\gamma$  over the EoS uncertainty for a fixed choice of  $\theta_{\text{m}}$ . Figure 8 shows the latter quantity for a simple mass distribution model where both binary component masses are sampled from the same Gaussian distribution with mean  $\mu_{\text{m}}$  and  $\sigma_{\text{m}}$ . We consider wide ranges for these parameters, that is  $1 \leq \mu_{\text{m}}/M_\odot \leq 2$  (encompassing the range of observed neutron star masses) and  $0.01 \leq \sigma_{\text{m}}/M_\odot \leq 0.5$  (from very narrow to very wide Gaussians over the considered mass range). The marginalisation over the EoS parameters is performed using our simplified two-parameter EoS dependence (§3.3), adopting the priors introduced in §3.4, limiting the NS masses to the range  $M_{1,2} \in [1M_\odot, M_{\text{TOV}}]$ . Filled contours show the result obtained using  $f_j = f_{j,\text{GW}}$ , while empty contours show the corresponding result when adopting the  $f_j = f_{j,\text{tot}}$  alternative constraint. This shows that a narrow ( $\sigma_{\text{m}} \lesssim 0.2M_\odot$ ) Gaussian distribution with  $\mu_{\text{m}} \lesssim 1.3M_\odot$  or  $\mu_{\text{m}} \gtrsim 1.6M_\odot$  is strongly disfavoured due to the very low implied jet incidence, given the available information on the EoS and the jet incidence, and consistently when using either of the constraints we considered (that is,  $\mathbf{d}_{\text{GW}}$  or  $\mathbf{d}_{\text{tot}}$ ). On the other hand, parameters representative of the main peak of the observed Galactic BNS population (white star in Fig. 8) are consistent with the constraints.

Given the fact that the analysis of GW-detected BNS (Abbott et al. 2021b; Landry & Read 2021), radio-detected Galactic BNS (Farrow et al. 2019) and both populations together (Galadage et al. 2021) currently disfavour a narrow-peaked mass distribution, we also tested a different parametric form, that is, a power law mass distribution model where both components are sampled from a power law  $P(m | \alpha, M_{\text{min}}, M_{\text{TOV}}) \propto m^\alpha$  with  $M_{\text{min}} \leq m \leq M_{\text{TOV}}$ , where  $m$  is the mass of either component. We consider a wide range of slopes  $-20 \leq \alpha \leq 10$ , and we take  $1 \leq M_{\text{min}}/M_\odot \leq 1.25$ , with the upper bound being limited by the lightest observed masses Galactic neutron stars (Farrow et al. 2019). Figure 9 shows the resulting constraint on the

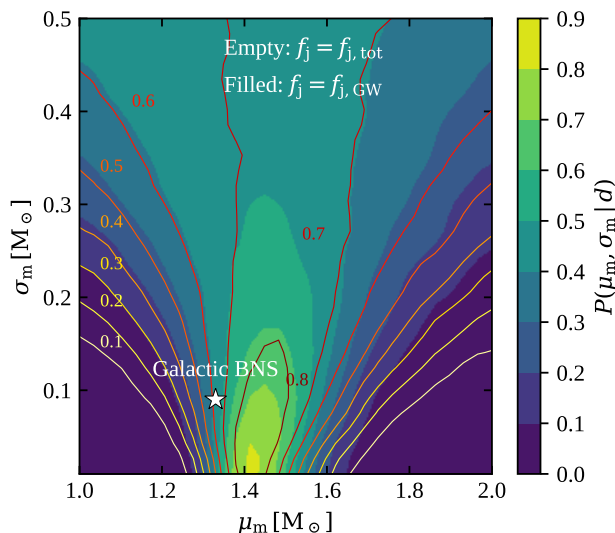


**Fig. 8.** Constraints on the parameters of a Gaussian BNS mass distribution model. Filled contours show the posterior probability density on the  $\mu_m$  (mean) and  $\sigma_m$  (standard deviation) parameters of a Gaussian mass distribution model (assuming random pairing) obtained using  $f_j = f_{j,\text{GW}}$ , i.e. the constraint based on the association of GW170817 and GRB170817A (§2). Empty contours show the corresponding result for  $f_j = f_{j,\text{tot}}$ , i.e. the constraint based on the relative SGRB and BNS local rate densities (§2.2). The white star marks parameter values  $(\mu_m, \sigma_m) = (1.33, 0.09) M_\odot$ , representative of the main peak of the observed Galactic BNS mass distribution (Özel & Freire 2016).

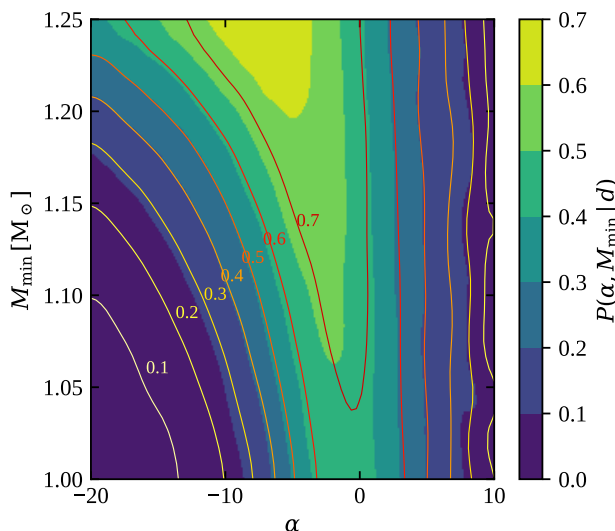


**Fig. 9.** Constraints on the parameters of a power law BNS mass distribution model. Colours and lines have the same meaning as in Fig. 8.

$(\alpha, M_{\text{min}})$  plane, with the same colour coding as for the Gaussian mass distribution.

It is instructive to project both results on the actual mass distribution space. We stress that we assume the component masses to be sampled from the same distribution (and randomly paired) which we refer to as  $P_m(m | \theta_m)$ . The implied

primary mass distribution is therefore

$$P(M_1 | \theta_m) = 2 \int P_m(M_1 | \theta_m) P_m(M_2 | \theta_m) \Theta(M_1 - M_2) dM_2, \quad (25)$$

and similarly for the secondary mass distribution. We keep the same uniform priors as in Figures 8 and 9, and we use the constraint on  $f_j = f_{j,\text{GW}}$ . Figure 10 shows the resulting mass distribution constraints. The credible bands in the figure are obtained as follows: we sampled the  $\theta_m$  posterior (computed according to Eq. 24) and constructed the  $P(m | \theta_m)$  curves corresponding to the samples. For each fixed value of  $m$ , the 50% (resp. 90%) credible band is comprised between the 25<sup>th</sup> and the 75<sup>th</sup> (resp. 5<sup>th</sup> and the 95<sup>th</sup>) percentiles of the values of these curves at  $m$ . Similarly, the thick solid lines represent the medians of these values. The cut-offs below  $1 M_\odot$  and above  $2.2 M_\odot$  are determined by our priors; in between this range, the result shows some improvement with respect to the priors and generally disfavours narrow mass distributions. The clearest feature, common to the two parametrisations (as is particularly visible in the comparison panel), is the requirement of a non-negligible probability for masses in the  $1.3 - 1.6 M_\odot$  range, which are particularly well-positioned in terms of satisfying our jet-launching conditions, as shown in Figure 7. This is in good agreement with the position and width of the main mass peak as found by Galaudage et al. (2021). In Appendix C we show a comparison of these results to those from the recently circulated preprint on the LIGO/Virgo GWTC-3 population study by Abbott et al. (2021b).

### 4.3. EoS constraints

The posterior in Eq. 23 can also be marginalised over the mass distribution parameters, to obtain constraints on the EoS given the knowledge of the mass distribution. Unfortunately, the current uncertainties on the jet incidence and mass distribution are too large, and this simply returns the EoS priors (which are already quite informative).

To give a basic illustration of the relevance of this kind of constraint in the future, we consider the following example. We adopt the power law mass distribution model described above, with a uniform prior on  $M_{\text{min}}$  between  $1.0 M_\odot$  and  $1.3 M_\odot$ , and a uniform prior on  $\alpha$  between  $-9$  and  $3.3$ , matching the 90% credible ranges from the GWTC-3 population study (Abbott et al. 2021b). This therefore roughly represents the current uncertainty on the NS mass distribution in merging stellar-mass compact object binaries. As a way of representing a hypothetical future in which the jet incidence is known with relatively small uncertainty, we assume the posterior probability on the jet incidence in GW-detectable binaries  $f_{j,\text{GW}}$  to be represented by a Gaussian with standard deviation  $\sigma_f = 0.05$  (which represents roughly a 6-fold improvement over the current uncertainty, see Fig. 1) and two possible mean values,  $\mu_f = 0.25$  and  $\mu_f = 0.75$ . Eq. 22 then becomes

$$P(\alpha, M_{\text{min}}, M_{\text{TOV}}, R_{1.4}, \xi_d | \mathbf{d}_{\text{GW}}) \propto \mathcal{N}_{\mu_f, \sigma_f}(\tilde{f}_{j,\text{GW}}) \pi(M_{\text{TOV}}, R_{1.4}, \xi_d) \pi(\alpha) \pi(M_{\text{min}}). \quad (26)$$

The marginalised distributions  $P(M_{\text{TOV}}, R_{1.4} | \mathbf{d}_{\text{GW}})$  for the two choices of  $\mu_f$  are shown in Figures 11 and 12. The results show that the posterior probability on the EoS parameters is sensitive to the value of  $f_{j,\text{GW}}$  even when the BNS mass distribution is relatively poorly known. We conclude that in the near

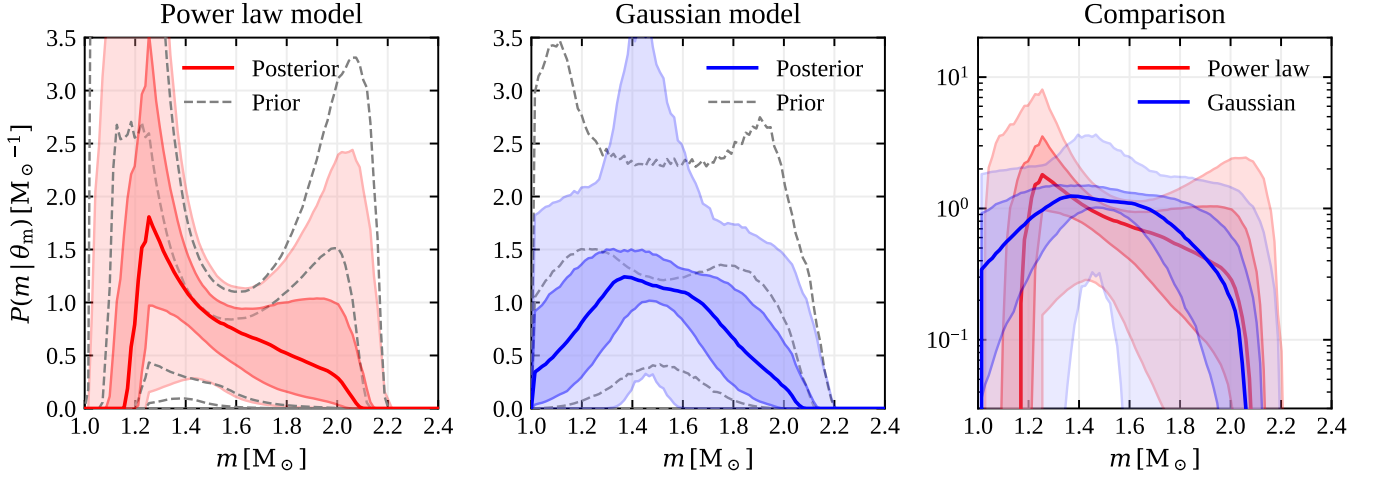


**Fig. 10.** Mass distribution constraint. In each panel, filled contours show the 90% and 50% credible regions of the probability distribution  $P(m | \theta_m)$  from which both  $M_1$  and  $M_2$  are sampled, while the thick solid line shows the median distribution at each  $m$ . The  $d_{j,GW}$  constraint is used. Grey dashed lines show the edges of the corresponding 90% and 50% credible regions when using only the priors. The left-hand panel shows the result for the power law mass distribution model, the central panel shows that for the Gaussian model, and the right-hand panel compares the two results with a log-scale vertical axis, to emphasise the lower 90% contour.

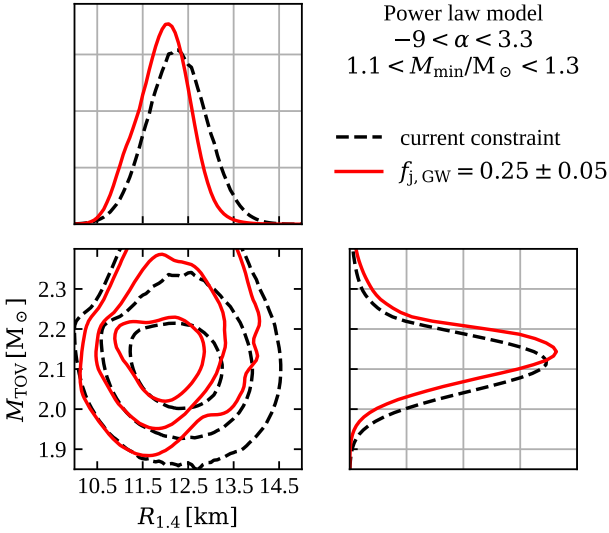


**Fig. 11.** Illustrative constraints on the EoS parameters assuming the power law mass distribution model with uniform priors on  $1.1 \leq M_{\min}/M_{\odot} \leq 1.3$  and  $-9 \leq \alpha \leq 3.3$ , matching the 90% credible ranges of the GWTC-3 NS mass distribution constraint (Abbott et al. 2021b), and using a hypothetical future constraint on the jet incidence  $P(f_{j,GW} | d_{GW}) \propto \mathcal{N}_{0.25,0.05}(f_{j,GW})$ .

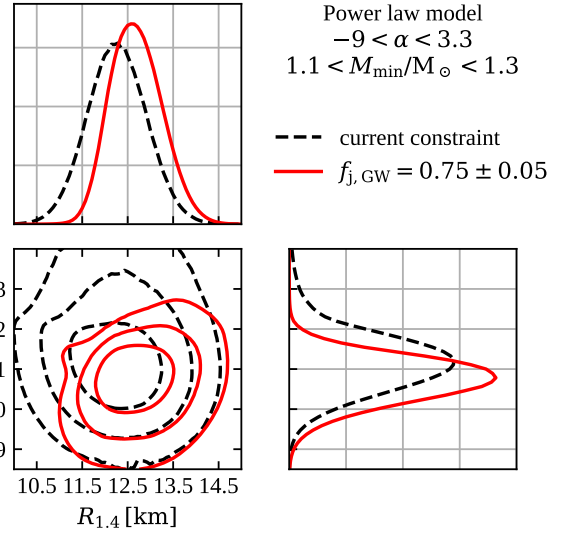


**Fig. 12.** Same as Figure 11, but assuming a jet incidence constraint with a different mean, that is  $P(f_{j,GW} | d_{tot}) \propto \mathcal{N}_{0.75,0.05}(f_{j,GW})$ .

future, when the BNS mass distribution (plus the local rate and possibly the jet incidence) will be better constrained thanks to more GW observations, this methodology will be able to place interesting constraints on the EoS parameters. This is in agreement with Fryer et al. 2015, who first discussed the possibility to constrain  $M_{TOV}$  from the jet incidence in GW-detectable BNS mergers.

## 5. Discussion and conclusions

The successful jet in GW170817 not only provided strong evidence in support of the long-held binary neutron star progenitor scenario for short gamma-ray bursts, but also clearly indicated that the launch of a relativistic jet is most likely a common outcome of this kind of mergers. In this work, we have shown how the fraction of BNS mergers that launch an ultra-relativistic jet can be used to place a joint constraint on the binary neutron star mass distribution and on the neutron star matter equation of state, under the assumption that the jet-launching mechanism requires the presence of an accretion disc with a non-negligible mass and the collapse of the merger remnant to a black hole within a fraction of a second (i.e. a

supra-massive or stable neutron star remnant are assumed not to yield SGRBs).

Based on the presence of a jet in GW170817 and adopting a simple binomial likelihood and a uniform prior, we derived a lower limit  $f_{j,GW} > 32\%$  (90% credible level) on the incidence of jets in GW-detected binary neutron stars. By comparing the lower limit on the local short gamma-ray burst rate density that can be placed by the detection of GRB170817A by *Fermi*/GBM and the local binary neutron star merger rate density estimated by Grunthal et al. (2021) based on Galactic double neutron stars, we constrained the jet incidence in the whole population to be  $f_{j,tot} > 20\%$ . This constraint is weaker than the finding of  $f_{j,tot} > 40\%$  (90% credible level) by Sarin et al. (2022), a pre-print – now published – that appeared while this work was nearing submission; however, the quantitative discrepancy is likely due to the reliance by Sarin et al. (2022) on the inferred local SGRB rate density estimated by Coward et al. (2012) and Wanderman & Piran (2015) – which most likely suffer from systematics due to the uncertain luminosity function (especially at the low end) and redshift distribution of events (see §2.2) – and their assumption that promptly collapsing BNS merger products without a significant accretion disc could still launch a jet and power a SGRB.

Comparing these results with the predicted jet incidence in a Blandford & Znajek (1977) jet-launching scenario, assuming equation of state priors informed by the latest multi-messenger constraints, we can exclude mass distributions with an overwhelming fraction of low-mass ( $\lesssim 1.3 M_{\odot}$ ) neutron stars (as predicted by many population synthesis models, especially those which adopt the Fryer et al. 2012 ‘rapid’ supernova prescription). This finding qualitatively agrees with Sarin et al. 2022 (their Figure 1). Similarly, a mass distribution dominated by high-mass ( $\gtrsim 1.6 M_{\odot}$ ) components is strongly disfavoured. We caution that this conclusion depends critically on the assumed jet-launching conditions: if an alternative magnetar central engine scenario (though theoretically less favoured) was adopted, these conclusion would be significantly altered.

The method can be also used in principle to place constraints on the equation of state, but the current data are insufficient to make this methodology competitive. Nevertheless, in §4.3 we provided a first illustration of how this will improve with future tighter constraints on the jet incidence.

Given the relatively weak constraints that we obtain with the currently available data, this work must be regarded primarily as a proof of concept. In the near future, several new binary neutron stars are expected (Abbott et al. 2020) to be detected through gravitational waves in the upcoming O4 and O5 observing runs of the GW detector network (which now includes KAGRA, Somiya 2012). In addition to that, new binary pulsars are being discovered in radio surveys (Han et al. 2021; Pan et al. 2021; Good et al. 2021; Agazie et al. 2021) at an increasing rate thanks to the steady improvements in both technology and data analysis techniques. Last, but not least, our understanding of selection effects that shape the properties of the observed radio pulsar population is advancing (Chattopadhyay et al. 2020). All these advances are going to positively impact the constraints on  $f_{j,GW}$  and  $f_{j,tot}$  (Fig. 1) and the  $\theta_m$  and  $\theta_{EoS}$  constraints that can be derived through the presented methodology.

New gravitational-wave detections of binary neutron star mergers will also open the possibility of directly using the information on the presence of a jet in each event (see Appendix A for an extension to uncertain jet associations) in population studies. In a modelling framework such as that de-

scribed by Mandel et al. (2019), the jet-launching condition (represented by the  $\Theta_j$  term, Eq. 16) could be used, in conjunction with the available information on the presence or absence of a jet in each GW-detected BNS merger, to constrain the parameters of single events in the population and, as a result, of global population parameters (i.e. hyperparameters) such as  $\theta_m$  and  $\theta_{EoS}$ . This can complement methods that exploit information on kilonova ejecta masses (Li & Paczyński 1998; Metzger 2019) and SGRB afterglow observations to augment the information that can be obtained from the gravitational-wave data (e.g. Hotokezaka et al. 2019; Radice & Dai 2019; Lazzati & Perna 2019; Barbieri et al. 2019; Coughlin et al. 2019; Dietrich et al. 2020; Breschi et al. 2021; Raaijmakers et al. 2021b). In this context, multi-messenger observations of BNS mergers close to the boundaries of the currently viable parameter space for jet launching would be particularly informative: as an example, the observation of a clear jet signature (or a tight constraint on its presence) in a system whose masses lie in the region where jet-launching is most uncertain (regions where  $P_j \sim 0.5$  in Fig. 7) would have the highest impact on the results that can be obtained with the presented method. Conversely, observations that clearly contradict the jet-launching conditions adopted in this work (such as a jet-less system with masses in the  $P_j \sim 1$  region in Fig. 7, or a jet-launching system with masses in the dark blue regions of the same figure) would point to the need for a revision in the assumed jet-launching conditions.

*Acknowledgements.* The authors thank the anonymous referee for a very detailed and insightful report that helped in improving the presentation of the results. The authors also thank Sylvia Biscoveanu and Samuele Ronchini for insightful comments and suggestions. OS thanks Giancarlo Ghirlanda, Monica Colpi, Michele Ronchi, Annalisa Celotti and Floor Broekgaarden for helpful comments and discussions. OS acknowledges financial support from the INAF-Prin 2017 (1.05.01.88.06) and the Italian Ministry for University and Research grants 1.05.06.13 and 20179ZF5KS. IM acknowledges support from the Australian Research Council Centre of Excellence for Gravitational Wave Discovery (OzGrav), through project number CE17010004. IM is a recipient of the Australian Research Council Future Fellowship FT190100574.

## References

- Aasi, J., Abbott, B. P., Abbott, R., & The LIGO Scientific Collaboration. 2015, *Classical and Quantum Gravity*, 32, 074001
- Abadie, J., Abbott, B. P., Abbott, R., LIGO Scientific Collaboration, & Virgo Collaboration. 2010, *Classical and Quantum Gravity*, 27, 173001
- Abbott, B. P., LIGO Scientific Collaboration, & Virgo Collaboration. 2018, *Phys. Rev. Lett.*, 121, 161101
- Abbott, B. P., LIGO Scientific Collaboration, & Virgo Collaboration. 2019, *Physical Review X*, 9, 011001
- Abbott, B. P., LIGO Scientific Collaboration, & Virgo Collaboration. 2020, *ApJ*, 892, L3
- Abbott, B. P., LIGO Scientific Collaboration, Virgo Collaboration, Fermi Gamma-ray Burst Monitor, & INTEGRAL. 2017, *ApJ*, 848, L13
- Abbott, B. P., LIGO Scientific Collaboration, Virgo Collaboration, & KAGRA Collaboration. 2020, *Living Reviews in Relativity*, 23, 3
- Abbott, B. P., The LIGO Scientific Collaboration, the Virgo Collaboration, & the KAGRA Collaboration. 2021a, arXiv e-prints, arXiv:2111.03606
- Abbott, B. P., The LIGO Scientific Collaboration, the Virgo Collaboration, & the KAGRA Collaboration. 2021b, arXiv e-prints, arXiv:2111.03634
- Abbott, R., the LIGO Scientific Collaboration, the Virgo Collaboration, & the KAGRA Collaboration. 2021a, *ApJ*, 915, L5
- Abbott, R., The LIGO Scientific Collaboration, the Virgo Collaboration, & the KAGRA Collaboration. 2021b, arXiv e-prints, arXiv:2111.03608
- Acernese, F., Agathos, M., Agatsuma, K., & The Virgo Collaboration. 2014, *Classical and Quantum Gravity*, 32, 024001
- Agazie, G. Y., Mingyar, M. G., McLaughlin, M. A., et al. 2021, *ApJ*, 922, 35
- Aguilera-Miret, R., Viganò, D., Carrasco, F., Miñano, B., & Palenzuela, C. 2020, *Phys. Rev. D*, 102, 103006
- Akmal, A., Pandharipande, V. R., & Ravenhall, D. G. 1998, *Phys. Rev. C*, 58, 1804

- Annala, E., Gorda, T., Katerini, E., et al. 2022, *Physical Review X*, 12, 011058
- Ascenzi, S., Oganessian, G., Salafia, O. S., et al. 2020, *A&A*, 641, A61
- Barbieri, C., Salafia, O. S., Colpi, M., Ghirlanda, G., & Perego, A. 2021, *A&A*, 654, A12
- Barbieri, C., Salafia, O. S., Perego, A., Colpi, M., & Ghirlanda, G. 2019, *A&A*, 625, A152
- Barkov, M. V., Luo, Y., & Lyutikov, M. 2021, *ApJ*, 907, 109
- Bauswein, A., Blacker, S., Lioutas, G., et al. 2021, *Phys. Rev. D*, 103, 123004
- Beniamini, P., Duque, R., Daigne, F., & Mochkovitch, R. 2020, *MNRAS*, 492, 2847
- Beniamini, P., Petropoulou, M., Barniol Duran, R., & Giannios, D. 2019, *MNRAS*, 483, 840
- Berger, E. 2014, *ARA&A*, 52, 43
- Bernardini, M. G., Campana, S., Ghisellini, G., et al. 2013, *ApJ*, 775, 67
- Bernardini, M. G., Margutti, R., Mao, J., Zaninoni, E., & Chincarini, G. 2012a, *A&A*, 539, A3
- Bernardini, M. G., Margutti, R., Zaninoni, E., & Chincarini, G. 2012b, *Memorie della Societa Astronomica Italiana Supplementi*, 21, 226
- Bernuzzi, S., Breschi, M., Daszuta, B., et al. 2020, *MNRAS*, 497, 1488
- Bernuzzi, S., Perego, A., & Zappa, F. 2018, *bns\_lum* git repository, [https://git.tpi.uni-jena.de/core/bns\\_lum](https://git.tpi.uni-jena.de/core/bns_lum), [Online; commit sha:a4c7fc8ce4b7826e58babe6fcc875155336a6602]
- Biscoveanu, S., Thrane, E., & Vitale, S. 2020, *ApJ*, 893, 38
- Blandford, R. D. & Znajek, R. L. 1977, *MNRAS*, 179, 433
- Bozzola, G., Espino, P. L., Lewin, C. D., & Paschalidis, V. 2019, *European Physical Journal A*, 55, 149
- Breschi, M., Perego, A., Bernuzzi, S., et al. 2021, *MNRAS*, 505, 1661
- Breu, C. & Rezzolla, L. 2016, *MNRAS*, 459, 646
- Broekgaarden, F. S., Berger, E., Neijssel, C. J., et al. 2021, *MNRAS*, 508, 5028
- Burns, E., Connaughton, V., Zhang, B.-B., et al. 2016, *ApJ*, 818, 110
- Burns, E., Svinikin, D., Hurley, K., et al. 2021, *ApJ*, 907, L28
- Burrows, A. & Lattimer, J. M. 1986, *ApJ*, 307, 178
- Chattopadhyay, D., Stevenson, S., Hurley, J. R., Rossi, L. J., & Flynn, C. 2020, *MNRAS*, 494, 1587
- Chen, H.-Y. & Holz, D. E. 2013, *Phys. Rev. Lett.*, 111, 181101
- Christie, I. M., Lalakos, A., Tchekhovskoy, A., et al. 2019, *MNRAS*, 490, 4811
- Ciolfi, R. 2020, *MNRAS*, 495, L66
- Ciolfi, R. & Kalinani, J. V. 2020, *ApJ*, 900, L35
- Clark, J., Evans, H., Fairhurst, S., et al. 2015, *ApJ*, 809, 53
- Colombo, A., Salafia, O. S., Gabrielli, F., et al. 2022, *arXiv e-prints*, [arXiv:2204.07592](https://arxiv.org/abs/2204.07592)
- Coughlin, M. W., Dietrich, T., Margalit, B., & Metzger, B. D. 2019, *MNRAS*, 489, L91
- Coward, D. M., Howell, E. J., Piran, T., et al. 2012, *MNRAS*, 425, 2668
- Cromartie, H. T., Fonseca, E., Ransom, S. M., et al. 2020, *Nature Astronomy*, 4, 72
- Dai, Z. G. & Lu, T. 1998, *A&A*, 333, L87
- Dall'Osso, S., Stratta, G., Guetta, D., et al. 2011, *A&A*, 526, A121
- D'Avanzo, P. 2015, *Journal of High Energy Astrophysics*, 7, 73
- Della Valle, M., Guetta, D., Cappellaro, E., et al. 2018, *MNRAS*, 481, 4355
- Dessart, L., Ott, C. D., Burrows, A., Rosswog, S., & Livne, E. 2009, *ApJ*, 690, 1681
- Dietrich, T., Coughlin, M. W., Pang, P. T. H., et al. 2020, *Science*, 370, 1450
- Dobie, D., Murphy, T., Kaplan, D. L., et al. 2021, *MNRAS*, 505, 2647
- Domink, M., Belczynski, K., Fryer, C., et al. 2012, *ApJ*, 759, 52
- Dudi, R., Dietrich, T., Rashti, A., et al. 2021, *arXiv e-prints*, [arXiv:2108.10429](https://arxiv.org/abs/2108.10429)
- Duffell, P. C. & MacFadyen, A. I. 2015, *ApJ*, 806, 205
- Duffell, P. C., Quataert, E., Kasen, D., & Klion, H. 2018, *ApJ*, 866, 3
- Duque, R., Beniamini, P., Daigne, F., & Mochkovitch, R. 2021, *arXiv e-prints*, [arXiv:2112.02917](https://arxiv.org/abs/2112.02917)
- East, W. E., Paschalidis, V., Pretorius, F., & Tsokaros, A. 2019, *Phys. Rev. D*, 100, 124042
- Eichler, D., Livio, M., Piran, T., & Schramm, D. N. 1989, *Nature*, 340, 126
- Farah, A., Essick, R., Doctor, Z., Fishbach, M., & Holz, D. E. 2020, *ApJ*, 895, 108
- Farrow, N., Zhu, X.-J., & Thrane, E. 2019, *ApJ*, 876, 18
- Fong, W., Berger, E., Margutti, R., & Zauderer, B. A. 2015, *ApJ*, 815, 102
- Fonseca, E., Cromartie, H. T., Pennucci, T. T., et al. 2021, *ApJ*, 915, L12
- Fryer, C. L., Belczynski, K., Ramirez-Ruiz, E., et al. 2015, *ApJ*, 812, 24
- Fryer, C. L., Belczynski, K., Wiktorowicz, G., et al. 2012, *ApJ*, 749, 91
- Galama, T. J., Vreeswijk, P. M., van Paradijs, J., et al. 1998, *Nature*, 395, 670
- Galaudage, S., Adamcewicz, C., Zhu, X.-J., Stevenson, S., & Thrane, E. 2021, *ApJ*, 909, L19
- Genet, F., Daigne, F., & Mochkovitch, R. 2007, *MNRAS*, 381, 732
- Ghirlanda, G., Salafia, O. S., Paragi, Z., et al. 2019, *Science*, 363, 968
- Ghirlanda, G., Salafia, O. S., Pescalli, A., et al. 2016, *A&A*, 594, A84
- Giacomazzo, B., Rezzolla, L., & Baiotti, L. 2009, *MNRAS*, 399, L164
- Goldstein, A., Veres, P., Burns, E., et al. 2017, *ApJ*, 848, L14
- Gompertz, B. P., O'Brien, P. T., Wynn, G. A., & Rowlinson, A. 2013, *MNRAS*, 431, 1745
- Good, D. C., Andersen, B. C., Chawla, P., et al. 2021, *ApJ*, 922, 43
- Goussard, J. O., Haensel, P., & Zdzunik, J. L. 1997, *A&A*, 321, 822
- Goussard, J. O., Haensel, P., & Zdzunik, J. L. 1998, *A&A*, 330, 1005
- Grunthal, K., Kramer, M., & Desvignes, G. 2021, *MNRAS*, 507, 5658
- Haensel, P., Zdzunik, J. L., Bejger, M., & Lattimer, J. M. 2009, *A&A*, 502, 605
- Han, J. L., Wang, C., Wang, P. F., et al. 2021, *Research in Astronomy and Astrophysics*, 21, 107
- Hayes, F., Heng, I. S., Veitch, J., & Williams, D. 2020, *ApJ*, 891, 124
- Hempel, M., Fischer, T., Schaffner-Bielich, J., & Liebendörfer, M. 2012, *ApJ*, 748, 70
- Hjorth, J., Levan, A. J., Tanvir, N. R., et al. 2017, *ApJ*, 848, L31
- Hogg, D. W. 1999, *arXiv e-prints*, astro
- Hosseinzadeh, G., Cowperthwaite, P. S., Gomez, S., et al. 2019, *ApJ*, 880, L4
- Hotokezaka, K., Nakar, E., Gottlieb, O., et al. 2019, *Nature Astronomy*, 3, 940
- Hotokezaka, K., Nissanke, S., Hallinan, G., et al. 2016, *ApJ*, 831, 190
- Jeffreys, H. 1946, *Proceedings of the Royal Society of London Series A*, 186, 453
- Just, O., Obergaulinger, M., Janka, H. T., Bauswein, A., & Schwarz, N. 2016, *ApJ*, 816, L30
- Kashyap, R., Das, A., Radice, D., et al. 2021, *arXiv e-prints*, [arXiv:2111.05183](https://arxiv.org/abs/2111.05183)
- Kawamura, T., Giacomazzo, B., Kastaun, W., et al. 2016, *Phys. Rev. D*, 94, 064012
- Kim, C., Kalogera, V., & Lorimer, D. R. 2003, *ApJ*, 584, 985
- Kiuchi, K., Cerdá-Durán, P., Kyutoku, K., Sekiguchi, Y., & Shibata, M. 2015, *Phys. Rev. D*, 92, 124034
- Kiuchi, K., Kyutoku, K., Sekiguchi, Y., & Shibata, M. 2018, *Phys. Rev. D*, 97, 124039
- Kiuchi, K., Kyutoku, K., Sekiguchi, Y., Shibata, M., & Wada, T. 2014, *Phys. Rev. D*, 90, 041502
- Kölsch, M., Dietrich, T., Ujevic, M., & Bruegmann, B. 2021, *arXiv e-prints*, [arXiv:2112.11851](https://arxiv.org/abs/2112.11851)
- Komissarov, S. S. 2001, *MNRAS*, 326, L41
- Kopparapu, R. K., Hanna, C., Kalogera, V., et al. 2008, *ApJ*, 675, 1459
- Kouveliotou, C., Meegan, C. A., Fishman, G. J., et al. 1993, *ApJ*, 413, L101
- Krüger, C. J. & Foucart, F. 2020, *Phys. Rev. D*, 101, 103002
- Kumar, P. & Zhang, B. 2015, *Phys. Rep.*, 561, 1
- Landry, P., Essick, R., & Chatziioannou, K. 2020, *Phys. Rev. D*, 101, 123007
- Landry, P. & Read, J. S. 2021, *ApJ*, 921, L25
- Lazzati, D. & Perna, R. 2019, *ApJ*, 881, 89
- Legred, I., Chatziioannou, K., Essick, R., Han, S., & Landry, P. 2021, *Phys. Rev. D*, 104, 063003
- Leventis, K., Wijers, R. A. M. J., & van der Horst, A. J. 2014, *MNRAS*, 437, 2448
- Li, L.-X. & Paczyński, B. 1998, *ApJ*, 507, L59
- Lira, M., Degollado, J. C., Moreno, C., & Núñez, D. 2022, *arXiv e-prints*, [arXiv:2201.02287](https://arxiv.org/abs/2201.02287)
- Liu, H.-Y. & Yu, Y.-W. 2019, *Research in Astronomy and Astrophysics*, 19, 118
- Lynch, R. S., Boyles, J., Ransom, S. M., et al. 2013, *ApJ*, 763, 81
- Madau, P. & Fragos, T. 2017, *ApJ*, 840, 39
- Mandel, I. & Broekgaarden, F. S. 2021, *arXiv e-prints*, [arXiv:2107.14239](https://arxiv.org/abs/2107.14239)
- Mandel, I., Farr, W. M., & Gair, J. R. 2019, *MNRAS*, 486, 1086
- Mapelli, M. & Giacobbo, N. 2018, *MNRAS*, 479, 4391
- Metzger, B. D. 2019, *Living Reviews in Relativity*, 23, 1
- Metzger, B. D., Giannios, D., Thompson, T. A., Bucciantini, N., & Quataert, E. 2011, *MNRAS*, 413, 2031
- Metzger, B. D., Quataert, E., & Thompson, T. A. 2008, *MNRAS*, 385, 1455
- Miller, M. C., Lamb, F. K., Dittmann, A. J., et al. 2019, *ApJ*, 887, L24
- Miller, M. C., Lamb, F. K., Dittmann, A. J., et al. 2021, *ApJ*, 918, L28
- Mochkovitch, R., Hernanz, M., Isern, J., & Martin, X. 1993, *Nature*, 361, 236
- Moharana, R. & Piran, T. 2017, *MNRAS*, 472, L55
- Mooley, K. P., Deller, A. T., Gottlieb, O., et al. 2018, *Nature*, 561, 355
- Mösta, P., Radice, D., Haas, R., Schnetter, E., & Bernuzzi, S. 2020, *ApJ*, 901, L37
- Norris, J. P. & Bonnell, J. T. 2006, *ApJ*, 643, 266
- Nousek, J. A., Kouveliotou, C., Grupe, D., et al. 2006, *ApJ*, 642, 389
- Obergaulinger, M., Aloy, M. A., & Müller, E. 2010, *A&A*, 515, A30
- Oganessian, G., Ascenzi, S., Branchesi, M., et al. 2020, *ApJ*, 893, 88
- Özel, F. & Freire, P. 2016, *ARA&A*, 54, 401
- Palenzuela, C., Aguilera-Miret, R., Carrasco, F., et al. 2021, *arXiv e-prints*, [arXiv:2112.08413](https://arxiv.org/abs/2112.08413)
- Pan, Z., Qian, L., Ma, X., et al. 2021, *ApJ*, 915, L28
- Pang, P. T. H., Tews, I., Coughlin, M. W., et al. 2021, *ApJ*, 922, 14
- Papenfort, L. J., Most, E. R., Tootle, S., & Rezzolla, L. 2022, *arXiv e-prints*, [arXiv:2201.03632](https://arxiv.org/abs/2201.03632)

- Pavan, L., Bordas, P., Pühlhofer, G., et al. 2014, A&A, 562, A122
- Perego, A., Rosswog, S., Cabezón, R. M., et al. 2014, MNRAS, 443, 3134
- Piro, A. L., Giacomazzo, B., & Perna, R. 2017, ApJ, 844, L19
- Planck Collaboration. 2016, A&A, 594, A13
- Pol, N., McLaughlin, M., & Lorimer, D. R. 2020, Research Notes of the American Astronomical Society, 4, 22
- Raaijmakers, G., Greif, S. K., Hebel, K., et al. 2021a, ApJ, 918, L29
- Raaijmakers, G., Greif, S. K., Riley, T. E., et al. 2020, ApJ, 893, L21
- Raaijmakers, G., Nissanke, S., Foucart, F., et al. 2021b, ApJ, 922, 269
- Raaijmakers, G., Riley, T. E., Watts, A. L., et al. 2019, ApJ, 887, L22
- Radice, D. & Dai, L. 2019, European Physical Journal A, 55, 50
- Rees, M. J. & Mészáros, P. 1998, ApJ, 496, L1
- Rezzolla, L., Most, E. R., & Weih, L. R. 2018, ApJ, 852, L25
- Rowlinson, A., O'Brien, P. T., Metzger, B. D., Tanvir, N. R., & Levan, A. J. 2013, MNRAS, 430, 1061
- Ruiz, M., Shapiro, S. L., & Tsokaros, A. 2018, Phys. Rev. D, 98, 123017
- Salafia, O. S., Barbieri, C., Ascenzi, S., & Toffano, M. 2020, A&A, 636, A105
- Salafia, O. S., Ghirlanda, G., Ascenzi, S., & Ghisellini, G. 2019, A&A, 628, A18
- Salafia, O. S. & Giacomazzo, B. 2021, A&A, 645, A93
- Sarin, N., Lasky, P. D., & Ashton, G. 2020, MNRAS, 499, 5986
- Sarin, N., Lasky, P. D., Vivanco, F. H., et al. 2022, Phys. Rev. D, 105, 083004
- Schutz, B. F. 2011, Classical and Quantum Gravity, 28, 125023
- Shibata, M., Zhou, E., Kiuchi, K., & Fujibayashi, S. 2019, Phys. Rev. D, 100, 023015
- Somiya, K. 2012, Classical and Quantum Gravity, 29, 124007
- Strang, L. C. & Melatos, A. 2019, MNRAS, 487, 5010
- Stratta, G., Dainotti, M. G., Dall'Osso, S., Hernandez, X., & De Cesare, G. 2018, ApJ, 869, 155
- Sun, H., Zhang, B., & Gao, H. 2017, ApJ, 835, 7
- Tan, W.-W. & Yu, Y.-W. 2020, ApJ, 902, 83
- Tchekhovskoy, A., Narayan, R., & McKinney, J. C. 2010, ApJ, 711, 50
- Thompson, C. 1994, MNRAS, 270, 480
- Thompson, T. A., Chang, P., & Quataert, E. 2004, ApJ, 611, 380
- Tootle, S. D., Papenfort, L. J., Most, E. R., & Rezzolla, L. 2021, ApJ, 922, L19
- Usov, V. V. 1992, Nature, 357, 472
- van den Eijnden, J., Degenaar, N., Russell, T. D., et al. 2018, Nature, 562, 233
- Vigna-Gómez, A., Neijssel, C. J., Stevenson, S., et al. 2018, MNRAS, 481, 4009
- Vigna-Gómez, A., Schröder, S. L., Ramirez-Ruiz, E., et al. 2021, ApJ, 920, L17
- Wanderman, D. & Piran, T. 2015, MNRAS, 448, 3026
- Williams, D., Clark, J. A., Williamson, A. R., & Heng, I. S. 2018, ApJ, 858, 79
- Woosley, S. E. 1993, ApJ, 405, 273
- Yagi, K. & Yunes, N. 2017, Phys. Rep., 681, 1
- Yamazaki, R. 2009, ApJ, 690, L118
- Zappa, F., Bernuzzi, S., Pannarale, F., Mapelli, M., & Giacobbo, N. 2019, Phys. Rev. Lett., 123, 041102
- Zappa, F., Bernuzzi, S., Radice, D., Perego, A., & Dietrich, T. 2018, Phys. Rev. Lett., 120, 111101
- Zhang, B., Fan, Y. Z., Dyks, J., et al. 2006, ApJ, 642, 354
- Zhang, B. & Mészáros, P. 2001, ApJ, 552, L35

## Appendix A: Inference on $f_{j,\text{GW}}$ from multiple observations with uncertain jets

In this appendix, we describe how the posterior probability on  $f_{j,\text{GW}}$  can be derived in presence of multiple observations, including cases in which the presence of a jet is uncertain. Let us assume that  $n$  events have been observed, and that we are able to estimate, for each  $i$ -th event, the probability  $P_{\text{miss},i}$  that a jet would have been missed (i.e. no conclusive statement can be made) if present: this will be typically a model-dependent estimate based on the (viewing-angle-dependent) expected jet emission properties, combined with information on the fraction of the BNS merger GW localisation volume that has been surveyed, and the depth of the available observations<sup>9</sup>. Without using other information (such as that on the single-event masses), the intrinsic probability of the presence of a jet in each GW-detected event is just  $f_{j,\text{GW}}$ . The likelihood of observing a jet in association to the  $i$ -th event is therefore  $P_{j,i} = f_{j,\text{GW}}(1 - P_{\text{miss},i})$ , while that of observing no jet is  $P_{\neg j,i} = (1 - f_{j,\text{GW}}) + f_{j,\text{GW}}P_{\text{miss},i} = 1 - P_{j,i}$ , so that we can write

$$P(J_i | f_{j,\text{GW}}, P_{\text{miss},i}) = J_i P_{j,i} + (1 - J_i)(1 - P_{j,i}), \quad (\text{A.1})$$

where  $J_i = 1$  if conclusive evidence in favour of a jet was found in association to the  $i$ -th event, and  $J_i = 0$  otherwise. The  $f_{j,\text{GW}}$  posterior, up to a normalization factor, is then

$$P(f_{j,\text{GW}} | \mathbf{J}, \mathbf{P}_{\text{miss}}) \propto \pi(f_{j,\text{GW}}) \prod_{i=1}^n P(J_i | f_{j,\text{GW}}, P_{\text{miss},i}), \quad (\text{A.2})$$

where  $\mathbf{J} = \{J_1, J_2, \dots, J_n\}$  and  $\mathbf{P}_{\text{miss}} = \{P_{\text{miss},1}, P_{\text{miss},2}, \dots, P_{\text{miss},n}\}$ . Let us evaluate Eq. A.2 in a concrete case, that of GW170817 and GW190425. In this setting, we have  $n = 2$  and  $\mathbf{J} = (1, 0)$ . Given the short distance to GW170817, its precise localization, and the availability of an extensive multi-wavelength dataset, including VLBI observations, we can set  $P_{\text{miss},1} \sim 0$ . In the case of GW190425, on the other hand, the poor GW sky localisation and larger distance hampered the detection and identification of a putative kilonova, which would have led to a precise localisation enabling deep multi-wavelength monitoring. For that reason, the available observations can only tentatively exclude an on-axis jet (Hosseinzadeh et al. 2019). In particular, gamma-ray upper limits set by *Fermi*/GBM, *INTEGRAL* and *Konus-Wind* (the latter covering the entire GW localization region of GW190425) can be interpreted as the indication that the viewing angle of a putative jet, if present, must have been sufficiently large. Assuming that any jet would have been missed beyond a limiting viewing angle  $\theta_{v,\text{lim}}$ , and calling  $P(\theta_v)$  the viewing angle probability

<sup>9</sup> We note that the available observations themselves could have been performed in an attempt to collect conclusive evidence in favour of a jet, in case preliminary observations provided promising indications of its presence. In that sense,  $P_{\text{miss}}$  can evolve as the data are collected and, in favourable cases such as GW170817, it can get close to zero (i.e. any jet in association to GW170817, if present, would not have been missed, also factoring in the indications towards a relatively small viewing angle that stem from kilonova observations, see e.g. Breschi et al. 2021). This latter statement clearly depends also on the assumed distribution of possible jet luminosities and properties in the probed bands.

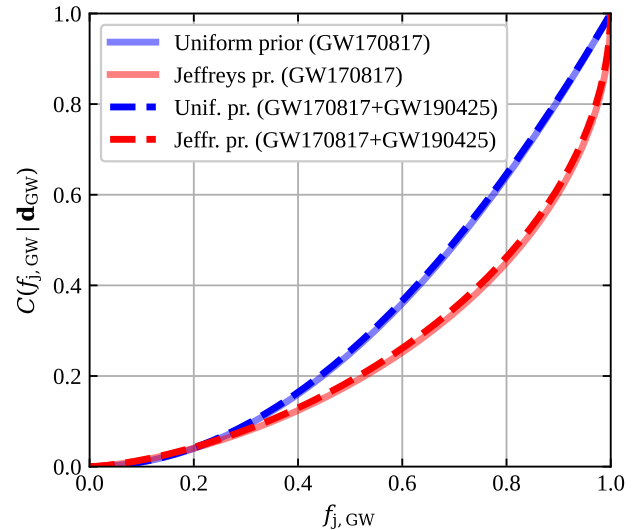


**Fig. A.1.** Cumulative posterior probability of the BNS jet incidence, showing the effect of adding GW190425 to the sample. The solid lines are the same as in Fig. 1 and account for GW170817 only, while the dashed ones account for GW190425 as well, as described in the text.

distribution of GW190425, a relativistic jet, if present, would have been missed with a probability

$$P_{\text{miss},2} \sim \int_{\theta_{v,\text{lim}}}^{\pi/2} P(\theta_v) d\theta_v. \quad (\text{A.3})$$

Using the probability distribution  $P(\theta_v)$  reconstructed<sup>10</sup> from the publicly available posterior samples (Abbott et al. 2020), and assuming  $\theta_{v,\text{lim}} = 0.2$  rad (a representative value for an SGRB beaming angle, Fong et al. 2015), we obtain  $P_{\text{miss},2} \simeq 0.94$ . This implies  $P(J_2 | f_{j,\text{GW}}, P_{\text{miss},2}) \simeq 1 - 0.06f_{j,\text{GW}}$ , which is the multiplicative correction to our result obtained by considering GW170817 only. The resulting posterior probability on  $f_{j,\text{GW}}$  is almost identical to the one obtained in §2, as can be appreciated from Figure A.1, which is unsurprising given the shallow available constraints on GW190425.

Given this framework, a relevant question that can be addressed is how many secure identifications of a jet, and/or how many tight limits on its presence, are needed to constrain  $f_{j,\text{GW}}$  to a desired precision. In that respect, we must keep in mind the fact that, while the presence of a jet can be assessed with relative certainty in favourable cases such as GW170817, its absence is generally much more difficult to prove, especially due to the strong relativistic beaming of radiation, which typically makes the detection of a putative jet extremely difficult beyond some limiting viewing angle. In well-localised cases, constraints from deep late-time radio observations can be used to probe a larger range of viewing angles, but for the majority of events this will not be a feasible route due to the combination of large localisation error box and low expected brightness of the late-time radio afterglow (e.g. Hotokezaka et al. 2016; Dobie et al. 2021; Colombo et al. 2022). This implies that it will be easier to constrain

<sup>10</sup> In low signal-to-noise ratio events such as GW190425, the posterior is well-approximated by the universal inclination angle distribution of GW-detected binaries of Schutz (2011). Indeed, using that distribution our result changes only by a few percent.

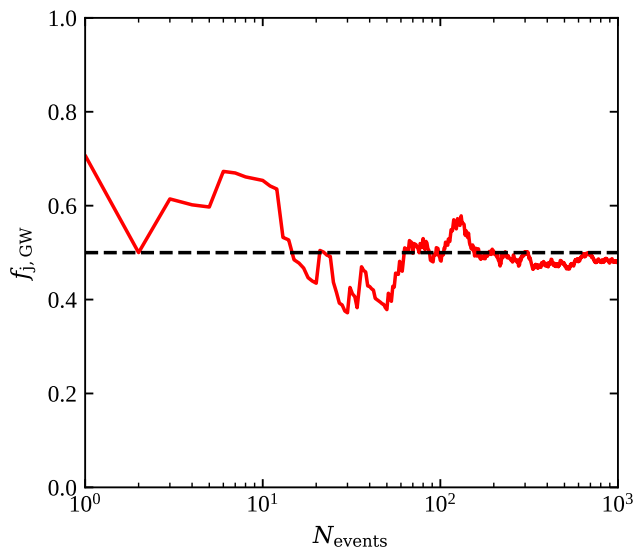


**Fig. A.2.**  $f_{j,GW}$  inference with multiple GW-detected BNS mergers. The coloured bands show the evolution of the posterior 90% and 50% credible range on  $f_{j,GW}$  after  $N_{\text{events}}$  simulated GW detections (see text), while the red solid line shows the median of the posterior. The horizontal black dashed line shows the true value.

$f_{j,GW}$  from below than from above. With these considerations in mind, we performed a simple experiment: we assumed a true value  $f_{j,GW,\text{true}} = 0.5$  and constructed a sample of mock BNS events with jets assigned randomly with probability  $f_{j,GW,\text{true}}$ . In order to represent in a simple way the jet detectability, for each event we randomly extracted a distance and an inclination from the universal joint distribution expected for GW-detected binaries (Schutz 2011). We then assumed a distance-dependent limiting viewing angle

$$\theta_{v,\text{lim}} = \min \left[ \frac{\pi}{2}, \left( \frac{d_L}{d_{L,e}} \right)^{-2} \right] \quad (\text{A.4})$$

beyond which observations are unable to constrain the presence, or absence, of a jet. Here  $d_{L,e}$  is a parameter, which we set equal to the 25th percentile of the simulated distances, so that only for the closest 25 percent of the events a jet can be excluded with 100% confidence if not present. If, for the  $i$ -th binary,  $\theta_v < \theta_{v,\text{lim}}$  and a jet was present, then we set  $J_i = 1$ ; in all other cases, we set  $J_i = 0$ . For all events, we computed  $P_{\text{miss},i}$  from Equations A.3 and A.4, therefore assuming that no detection can be made beyond  $\theta_{v,\text{lim}}$ , no matter how extensive the observations. Figure A.2 shows how the posterior probability on  $f_{j,GW}$  evolves as we include an increasing number  $N_{\text{events}}$  of these simulated events in the inference. The result suggests that several tens of detections are needed to be able to constrain the jet incidence to within 10-20%, and hundreds to get to a few percent constraint.

## Appendix B: Local rate density of GRB170817A-like sources

To estimate the local SGRB rate based on GRB170817A, we model the *Fermi* Gamma-ray Burst Monitor (GBM) detection of GRB170817A-like sources (i.e. sources with exactly the same luminosity and intrinsic gamma-ray spectrum as GRB170817A) as a Poisson process with an expected event

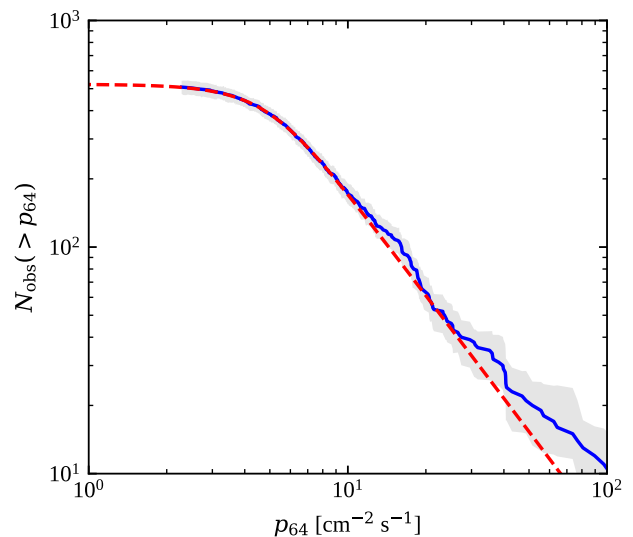


**Fig. B.1.** *Fermi*/GBM observed inverse cumulative distribution of 64-ms-binned photon fluxes in the 10-1000 keV band (blue solid line, with the grey band showing the 90% confidence band due to Poisson and measurement uncertainties), compared with our best-fitting model, Eq. B.4, with  $\alpha = 5.42$  and  $p_{\frac{1}{2}} = 2.25 \text{ ph cm}^{-2} \text{ s}^{-1}$  (red dashed line). The slight excess over the  $p_{64}^{-3/2}$  expected trend at high fluxes is likely due to contamination of the sample by magnetar giant flares in local galaxies (Burns et al. 2021).

number  $\lambda = R_0 V_{\text{eff}} T$  over a time  $T = 13 \text{ yr}$  (the current duration of the GBM survey), where  $V_{\text{eff}}$  is the GBM effective sensitive volume. The posterior probability on  $R_0$ , assuming a single detection, is

$$P(R_0 | 1) \propto P(1 | R_0) \pi(R_0) \quad (\text{B.1})$$

where  $P(1 | R_0) \propto R_0 \exp(-R_0 V_{\text{eff}} T)$  and we adopt the Jeffreys prior  $\pi(R_0) \propto R_0^{-1/2}$ . We estimate the effective sensitive volume as

$$V_{\text{eff}} = \eta_{\text{GBM}} \int_0^\infty \frac{1}{1+z} \frac{dV}{dz} P_{\text{det}}(z) dz \quad (\text{B.2})$$

where  $\eta_{\text{GBM}} = 0.59$  accounts for the GBM field of view and duty cycle (Burns et al. 2016),  $dV/dz$  is the differential comoving volume (Hogg 1999), the  $(1+z)^{-1}$  factor accounts for cosmological time dilation and  $P_{\text{det}}(z)$  represents the probability for GBM to detect a GRB170817A-like source at a redshift  $z$  within its field of view. In order to compute this quantity, we assume for simplicity that the GBM detection probability depends only on the peak photon flux  $p_{64}$  of the GRB, measured with a 64 ms binning, in the 10-1000 keV band, so that  $P_{\text{det}}(z) = P_{\text{det}}(p_{64}(z))$ . We then make the ansatz

$$P_{\text{det}}(p_{64}, \alpha, p_{\frac{1}{2}}) = \frac{1}{2} \left\{ 1 + \tanh \left[ \alpha \ln \left( \frac{p_{64}}{p_{\frac{1}{2}}} \right) \right] \right\}, \quad (\text{B.3})$$

which is a smooth function satisfying  $P_{\text{det}} = 1/2$  when  $p_{64} = p_{\frac{1}{2}}$ ,  $P_{\text{det}} \sim 1$  when  $p_{64} \gg p_{\frac{1}{2}}$  and  $P_{\text{det}} \sim 0$  when  $p_{64} \ll p_{\frac{1}{2}}$ . The  $\alpha$  parameter controls the sharpness of the transition from 0 to 1. To fix  $\alpha$  and  $p_{\frac{1}{2}}$ , we proceed as follows. We assume the intrinsic inverse cumulative distribution of short



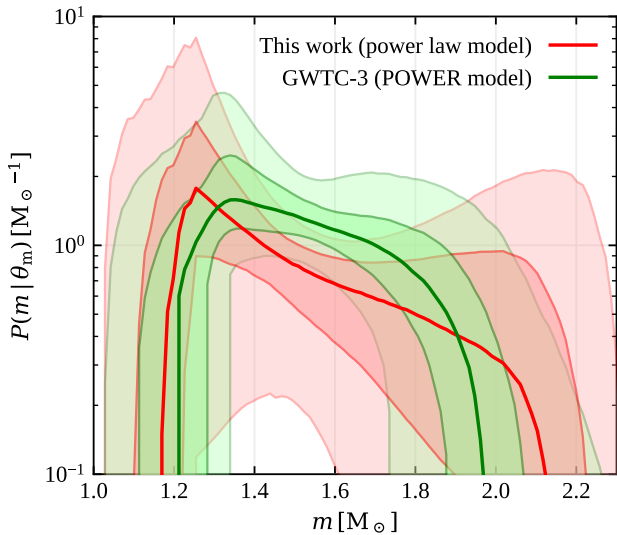


**Fig. C.1.** Comparison of our neutron star mass distribution posterior (power law model) with the GWTC-3 result from the population study described in Abbott et al. 2021b (their POWER model). Shaded areas show the 90% and 50% credible regions, while thick solid lines show the medians. Red is for our result (§4.2), blue is for the GWTC-3.

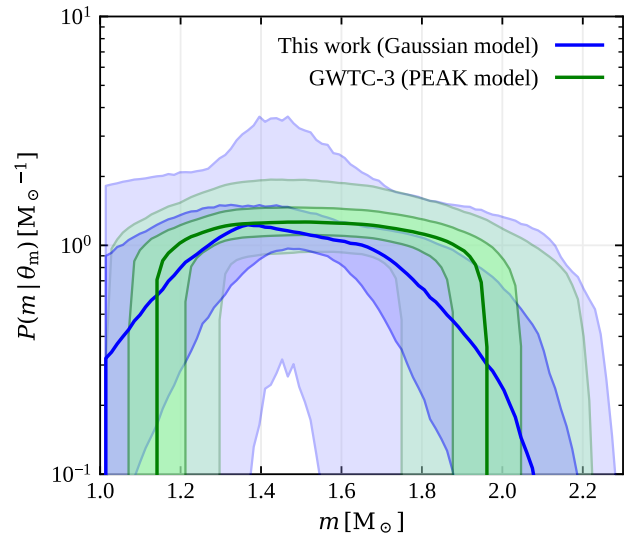


**Fig. C.2.** Same as Figure C.1, but for our Gaussian model and the GWTC-3 population study PEAK model.

GRB photon fluxes to follow  $N_{\text{int}}(> p_{64}) \propto p_{64}^{-3/2}$ , as expected for uniformly distributed sources in Euclidean space, in absence of evolution of the luminosity function with distance (which is reasonable as the typical redshifts are well below 1). The observed distribution is then

$$N_{\text{obs}}(> p_{64}, \alpha, p_{\frac{1}{2}}) \propto \int_{p_{64}}^{\infty} P_{\text{det}}(p, \alpha, p_{\frac{1}{2}}) \frac{dN_{\text{int}}}{dp}(p) dp. \quad (\text{B.4})$$

We fit the resulting distribution to that constructed with the actual *Fermi*/GBM catalog data (restricted to events with  $t_{90} \leq 2$  s) by minimizing the sum of the squares of the residuals, obtaining  $\alpha = 5.42$  and  $p_{\frac{1}{2}} = 2.25 \text{ ph cm}^{-2} \text{ s}^{-1}$ . The observed and modelled distributions are shown in Figure B.1.

Given the GRB170817A measured (Goldstein et al. 2017) peak photon flux  $p_{64} = 3.7 \text{ ph cm}^{-2} \text{ s}^{-1}$ , the best-fitting spectral model at the peak (second line of table 3 in Goldstein et al. 2017), the best-fitting host galaxy luminosity distance (Hjorth et al. 2017)  $d_L = 41 \text{ Mpc}$ , and assuming Planck cosmological parameters (Planck Collaboration 2016), we can compute the 64 ms photon flux of an identical source at any redshift,  $p_{64}(z)$ . This allows us to compute the integral in Eq. B.2, yielding  $V_{\text{eff}} = 1.13 \times 10^5 \text{ Mpc}^3$ . Plugging this in Eq. B.1, we obtain the posterior probability distribution shown in Figure 2, whose peak and 90% credible interval are  $R_0 = 342_{-337}^{+1798} \text{ Gpc}^{-3} \text{ yr}^{-1}$ , in good agreement with the simpler estimate by Della Valle et al. (2018).

## Appendix C: Comparison with GWTC-3

Figures C.1 and C.2 show comparisons of our mass distribution posteriors with the results from Abbott et al. (2021b) based on GWTC-3 (Abbott et al. 2021a) data. As a cautionary note, the definitions in our power law model match those of the POWER model from the GWTC-3 population study

(Fig. C.1), but their PEAK model has the minimum mass cut  $M_{\text{min}}$  as an additional free parameter (while ours is fixed at  $1 M_{\odot}$ ). Despite being significantly shallower, our constraints are in general agreement with those from the population study.